The Astrophysical Journal, 681:1183–1204, 2008 July 10


# METALLICITY CALIBRATIONS AND THE MASS-METALLICITY RELATION FOR STAR-FORMING GALAXIES

Lisa J. Kewley[1]
Institute of Astronomy, University of Hawaii, Honolulu, HI 96822; kewley@ifa.hawaii.edu

and

Sara L. Ellison
Department of Physics and Astronomy, University of Victoria, Victoria, BC V8W 3P6, Canada
*Received 2007 July 1; accepted 2007 December 22*

## ABSTRACT

We investigate the effect of metallicity calibrations, AGN classification, and aperture covering fraction on the local mass-metallicity (*M-Z*) relation using 27,730 star-forming galaxies from the SDSS Data Release 4. We analyze the SDSS *M-Z* relation with 10 metallicity calibrations, including theoretical and empirical methods. We show that the choice of metallicity calibration has a significant effect on the shape and *y*-intercept [$12 + \log(\mathrm{O/H})$] of the *M-Z* relation. The absolute metallicity scale (*y*-intercept) varies up to $\Delta[\log(\mathrm{O/H})] = 0.7$ dex, depending on the calibration used, and the change in shape is substantial. These results indicate that it is critical to use the same metallicity calibration when comparing different luminosity-metallicity or *M-Z* relations. We present new metallicity conversions that allow metallicities that have been derived using different strong-line calibrations to be converted to the same base calibration. These conversions facilitate comparisons between different samples, particularly comparisons between galaxies at different redshifts for which different suites of emission lines are available. Our new conversions successfully remove the large 0.7 dex discrepancies between the metallicity calibrations, and we reach agreement in the *M-Z* relation to within 0.03 dex on average. We investigate the effect of AGN classification and aperture covering fraction on the *M-Z* relation. We find that different AGN classification methods have negligible effect on the SDSS *M-Z* relation. We compare the SDSS *M-Z* relation with nuclear and global relations from the NFGS. The turnover of the *M-Z* relation at $M_* \sim 10^{10}\ M_\odot$ depends on the aperture covering fraction. We find that a lower redshift limit of $z < 0.04$ is insufficient for avoiding aperture effects in fiber spectra of the highest stellar mass ($M_* > 10^{10}\ M_\odot$) galaxies.

*Subject headings:* galaxies: abundances — galaxies: fundamental parameters — galaxies: spiral — galaxies: starburst — techniques: spectroscopic

## 1. INTRODUCTION

The relationship between metallicity and stellar mass provides crucial insight into galaxy formation and evolution. Theory predicts that as time progresses, the mean stellar metallicity of galaxies increases with age as galaxies undergo chemical enrichment, while the stellar mass of a galaxy will increase with time as galaxies are built through merging processes (e.g., Pei & Fall 1995; Somerville & Primack 1999; Somerville et al. 2000; Nagamine et al. 2001; Calura et al. 2004 and references therein). A correlation between mass and metallicity arises if low-mass galaxies have larger gas fractions than higher mass galaxies, as is observed in local galaxies (McGaugh & de Blok 1997; Bell & de Jong 2000; Boselli et al. 2001). The detailed relationship between metallicity and mass may depend critically on galactic-scale outflows driven by supernovae and stellar winds (for a review see, e.g., Garnett 2002; Pettini 2002). Thus, robust measurements of the mass-metallicity (*M-Z*) relation may provide important clues into the impact of galactic-scale winds on the chemical history of galaxies.

The *M-Z* relation was first observed in irregular and blue compact galaxies (Lequeux et al. 1979; Kinman & Davidson 1981). In subsequent work, luminosity was often used as a surrogate for mass because obtaining reliable mass estimates for galaxies was nontrivial. Rubin et al. (1984) provided the first evidence that metallicity is correlated with luminosity in disk galaxies. Further investigations solidified the correlation between luminosity and metallicity in nearby disk galaxies (Bothun et al. 1984; Wyse & Silk 1985; Skillman et al. 1989; Vila-Costas & Edmunds 1992; Zaritsky et al. 1994, hereafter Z94; Garnett 2002). However, optical luminosity may not be a reliable surrogate for the stellar mass of a galaxy because optical luminosities are sensitive to the level of current star formation and are extinguished by dust. Near-infrared luminosities can be influenced by the age of the stellar population of a galaxy. Fortunately, reliable stellar mass estimates are now possible, thanks to new state-of-the-art stellar evolutionary synthesis models (e.g., Silva et al. 1998; Leitherer et al. 1999; Fioc & Rocca-Volmerange 1999; Bruzual & Charlot 2003).

Key insight into the *M-Z* relation has recently been obtained with large spectroscopic surveys such as the Sloan Digital Sky Survey (SDSS) and the Two Degree Field Galaxy Redshift Survey (2dFGRS; e.g., Baldry et al. 2002; Schulte-Ladbeck et al. 2003; Lamareille et al. 2004; Tremonti et al. 2004, hereafter T04; Gallazzi et al. 2005). Using the SDSS stellar masses, T04 characterized the local *M-Z* relation for ~53,000 local galaxies. The *M-Z* relation is steep for masses $\lesssim 10^{10.5}\ M_\odot$ and flattens at higher masses. T04 use chemical evolution models to interpret this flattening in terms of efficient galactic-scale winds that remove metals from low-mass galaxies ($M \lesssim 10^{10.5}\ M_\odot$). Hierarchical galaxy formation models that include chemical evolution and feedback processes can reproduce the observed *M-Z* relation (De Lucia et al. 2004; de Rossi et al. 2007; Finlator & Dave 2008). However, these models rely on free parameters, such as feedback efficiency, that are relatively unconstrained by observations. Alternative scenarios proposed to explain the *M-Z* relation include low star

[1] Hubble Fellow.

formation efficiencies in low-mass galaxies caused by supernova feedback (Brooks et al. 2007) and a variable integrated stellar initial mass function (IMF; Köppen et al. 2007).

The advent of large 8–10 m telescopes and efficient multiobject spectrographs enables the luminosity-metallicity (*L-Z*) and, in some cases, the *M-Z* relation to be characterized to high redshifts (Kobulnicky et al. 1999, 2003; Carollo & Lilly 2001; Pettini et al. 2001; Lilly et al. 2003; Kobulnicky & Kewley 2004, hereafter KK04; Shapley et al. 2004; Maier et al. 2004, 2005, 2006; Liang et al. 2004, 2006; Hoyos et al. 2005; Savaglio et al. 2005; Mouhcine et al. 2006; Erb et al. 2006). Evolution in the *L-Z* and *M-Z* relations is now predicted by semianalytic models of galaxy formation within the ΛCDM framework that include chemical hydrodynamic simulations (De Lucia et al. 2004; Tissera et al. 2005; de Rossi et al. 2007; Davé & Oppenheimer 2007). Therefore, reliable observational estimates of the *L-Z* and *M-Z* relations may provide important constraints on galaxy evolution theory.

Reliable *M-Z* relations require a robust metallicity calibration. Common metallicity calibrations are based on metallicity-sensitive optical emission line ratios. These calibrations include theoretical methods based on photoionization models (for a review see, e.g., Kewley & Dopita 2002, hereafter KD02), empirical methods based on measurements of the electron temperature of the gas (e.g., Pilyugin 2001, hereafter P01; Pettini & Pagel 2004, hereafter PP04), or a combination of the two (e.g., Denicoló et al. 2002, hereafter D02). Comparisons among the metallicities estimated using these methods reveal large discrepancies (e.g., P01; Bresolin et al. 2004; Garnett et al. 2004b). These discrepancies usually manifest as a systematic offset in metallicity estimates, with high values estimated by theoretical calibrations and lower metallicities estimated by electron temperature metallicities. Such offsets are found to be as large as 0.6 dex in log (O/H) units (Liang et al. 2006; Yin et al. 2007b) and may significantly affect the shape and zero point of the *M-Z* or *L-Z* relations.

Initial investigations into the extent of these discrepancies have recently been made by Liang et al. (2006), Yin et al. (2007a, 2007b), and Nagao et al. (2006). Liang et al. (2006) applied the metallicity calibrations from four authors to ∼40,000 galaxies from the SDSS. They showed that calibrations based on electron temperature metallicities produce discrepant metallicities when compared with calibrations based on photoionization models. Yin et al. (2007b) compared the theoretical metallicities derived by T04 with $T_e$-based metallicities from P01 and Pilyugin & Thuan (2005, hereafter P05). They found a discrepancy of $\Delta[\log(\mathrm{O/H})] = 0.2$ dex between the two $T_e$-based metallicities and a larger discrepancy of $\Delta[\log(\mathrm{O/H})] = 0.6$ dex between the $T_e$-based methods and the theoretical method. Similar results were obtained by Yin et al. (2007a), who extended the Liang et al. (2006) work to low metallicities typical of low-mass galaxies.

The cause of the metallicity calibration discrepancies remains unclear. The discrepancy has been attributed to either an unknown problem with the photoionization models (Kennicutt et al. 2003) or temperature gradients or fluctuations that may cause metallicities based on the electron temperature method to underestimate the true metallicities (Stasińska 2002, 2005; Bresolin 2006). Until this discrepancy is resolved, the absolute metallicity scale is uncertain.

The metallicity discrepancy issue highlights the need for an in-depth study into the effect of metallicity calibration discrepancies and other effects on the *M-Z* relation. In this paper we investigate the robustness of the local *M-Z* relation for star-forming galaxies. We focus on three important factors that may influence the shape, *y*-intercept, and scatter of the *M-Z* relation: choice of metallicity calibration, aperture covering fraction, and active galactic nucleus (AGN) removal method. Our sample selection is described in § 2. We describe the stellar mass estimates and metallicities in §§ 3 and 4, respectively. We compare the *M-Z* relation derived using 10 different, popular metallicity calibrations in § 5. We find larger discrepancies between the *M-Z* relations derived with different metallicity calibrations than previously found. We calibrate the discrepancies between the different calibrations using robust fits, and we provide conversion relations for removing these discrepancies in § 6. We show that our new conversions successfully remove the large metallicity discrepancies in the *M-Z* relation. We investigate the effect of different schemes for AGN removal in § 7, and we determine the effect of fiber covering fraction in § 8. We discuss the impact of our results on the *M-Z* and *L-Z* relations in § 9. Our conclusions are given in § 10. In Appendices A and B we provide detailed descriptions of the metallicity calibrations used in this study and worked examples of the application of our conversions. Throughout this paper we adopt the flat Λ-dominated cosmology as measured by the *WMAP* experiment ($h = 0.72$, $\Omega_m = 0.29$; Spergel et al. 2003).

## 2. SAMPLE SELECTION

We selected our sample from the SDSS Data Release 4 (DR4) according to the following criteria:

1. Signal-to-noise ratio (S/N) of at least 8 in the strong emission lines [O II] λλ3726, 3729, Hβ, [O III] λ5007, Hα, [N II] λ6584, and [S II] λλ6717, 6731. An S/N > 8 is required for reliable metallicity estimates using established metallicity calibrations (Kobulnicky et al. 1999). For each line, we define the S/N as the ratio of the statistical error on the flux to the total flux, where the statistical errors are calculated by the SDSS pipeline described in T04.
2. Fiber covering fraction >20% of the total photometric $g'$-band light. We use the raw DR4 fiber and Petrosian magnitudes to calculate the fiber covering fraction. Kewley et al. (2005) found that a flux covering fraction >20% is required for metallicities to begin to approximate global values. Lower covering fractions can produce significant discrepancies between fixed-size aperture and global metallicity estimates. A covering fraction of >20% corresponds to a lower redshift limit of $z > 0.04$ for normal star-forming galaxies observed through the 3″ SDSS fibers. Large, luminous star-forming galaxies require a larger redshift to satisfy the covering fraction >20% requirement. We investigate residual aperture effects in § 8.
3. Upper redshift limit $z < 0.1$. The SDSS star-forming sample becomes incomplete at redshifts above $z > 0.1$ (see, e.g., Kewley et al. 2006, hereafter K06). With this upper redshift limit, the median redshift of our sample is $z \sim 0.068$.
4. Stellar mass estimates must be available. Stellar masses were derived by Kauffmann et al. (2003, hereafter K03) and T04.

We remove galaxies containing AGNs from our sample using the optical classification criteria given in K06. This classification scheme utilizes optical strong-line ratios to segregate galaxies containing AGNs from galaxies dominated by star formation. A total of 84% of the members of the SDSS sample satisfying our selection criteria are star forming according to the K06 classification scheme. This fraction of star-forming galaxies differs from the fraction in K06 because we apply a more stringent S/N cut, which removes many low-ionization nuclear emission-line regions (LINERs) prior to classification. In § 7 we investigate different AGN classification schemes and their effect on the shape of the *M-Z* relation.

The resulting sample contains 27,730 star-forming galaxies and does not include duplicates found in the original DR4 catalog. We note that our sample is smaller than the T04 sample because

we apply a more stringent S/N criterion and a stricter redshift range (T04 apply a redshift range of $0.005 < z < 0.25$).

We use the publicly available emission-line fluxes that were calculated by the MPA/JHU group (described in T04). These emission-line fluxes were calculated using a sophisticated code that is optimized for use with the SDSS galaxy spectra. This code applies a least-squares fit of the Bruzual & Charlot (2003) stellar population synthesis models and dust attenuation to the stellar continuum. Once the continuum has been removed, the emission-line fluxes are fitted with Gaussians, constraining the width and velocity separation of the Balmer lines together, and similarly for the forbidden lines.

We correct the emission-line fluxes for extinction using the Balmer decrement and the Cardelli et al. (1989) reddening curve. We assume an $R_V = A_V/E(B-V) = 3.1$ and an intrinsic H$\alpha$/H$\beta$ ratio of 2.85 (the Balmer decrement for case B recombination at $T = 10^4$ K and $n_e \sim 10^2$–$10^4$ cm$^{-3}$; Osterbrock 1989). A total of 539 galaxies in our sample (2%) have Balmer decrements less than the theoretical value. A Balmer decrement less than the theoretical value can result from an intrinsically low reddening combined with errors in the stellar absorption correction and/or errors in the line flux calibration and measurement. For the S/N of our data, the lowest $E(B-V)$ measurable is 0.01. We therefore assign these 539 galaxies an upper limit of $E(B-V) < 0.01$.

To investigate aperture effects (§ 8), we compare the SDSS *M-Z* relation with the *M-Z* relation derived from the Nearby Field Galaxy Survey (NFGS; Jansen et al. 2000a, 2000b). Jansen et al. (2000b) selected the NFGS objectively from the CfA1 redshift survey (Davis & Peebles 1983; Huchra et al. 1983) to approximate the local galaxy luminosity function (e.g., Marzke et al. 1994). The 198 galaxy NFGS sample contains the full range in Hubble type and absolute magnitude present in the CfA1 galaxy survey.

Jansen et al. (2000a) provide integrated and nuclear spectrophotometry for almost all galaxies in the NFGS sample. The covering fraction and metallicities of the nuclear and global spectra for the NFGS are described in Kewley et al. (2005). The nuclear $B_{26}$ covering fraction ranges between 0.4% and 72%, with an average nuclear covering fraction of 10% ± 11%.[2] The covering fraction of the integrated (global) spectra is between 52% and 97% of the *B*-band light, with an average of 82% ± 7%.

We apply the same extinction correction and AGN removal scheme to our NFGS supplementary sample as applied to the SDSS sample. In the NFGS sample, 121/198 galaxies can be classified using their narrow emission lines according to the K06 classification scheme. Of these, 106/121 (88%) are dominated by their star formation. The NFGS integrated metallicities have been published by Kewley et al. (2004) for several metallicity calibrations.

## 3. STELLAR MASS ESTIMATES

The SDSS stellar masses were derived by T04 and K03 using a combination of *z*-band luminosities and Monte Carlo stellar population synthesis fits to the 4000 Å break and the stellar Balmer absorption line H$\delta_A$. The model fits to the 4000 Å break and H$\delta_A$ provide powerful constraints on the star formation history and metallicity of each galaxy, thus providing a more reliable indicator of mass than assuming a simple mass-to-light ratio and a Kroupa (2001) IMF. Drory et al. (2004) recently compared these spectroscopic masses for ~17,000 SDSS galaxies with (1) masses derived from population synthesis fits to the broadband SDSS and Two Micron All Sky Survey (2MASS) colors and (2) masses calculated from SDSS velocity dispersions and effective radii. They concluded that the three methods for estimating mass agree to within ~0.2 dex over the $10^8$–$10^{12}$ $M_\odot$ range.

An alternative method for estimating mass was proposed by Bell & de Jong (2001). Bell & de Jong (2001) used stellar population synthesis models to compute prescriptions for converting optical colors and photometry into stellar masses assuming a scaled Salpeter (1955) IMF. This method is useful when near-IR colors are not available and spectral S/N is insufficient for reliable 4000 Å break and H$\delta_A$ measurements. We calculate masses for the NFGS galaxies by combining 2MASS *J*-band magnitudes with the $B-R$ colors (R. Jansen 2005, private communication). For all filters, we use "total" magnitudes, i.e., the integrated light based on extrapolated radial surface brightness fits. We apply a search radius of 5″ in the 2MASS database, resulting in matches for 85/106 star-forming galaxies. We calculate stellar masses using the models of Bell & de Jong (2001) as parameterized by Rosenberg et al. (2005). For the comparison between the SDSS and NFGS stellar masses (§ 8), we assume a Salpeter IMF and apply factors of 1.82 and 1.43 to the SDSS (Kroupa) and NFGS (scaled Salpeter) stellar masses, respectively (K03; Bell & de Jong 2001).

Recently, Kannappan & Gawiser (2007) compared stellar masses derived using stellar population synthesis fits to the NFGS spectra with masses derived using several methods, including the Bell & de Jong (2001) method. Kannappan & Gawiser (2007) find that the Bell & de Jong (2001) stellar mass prescription gives stellar masses that are ~1.5 times the population synthesis approach (see Kannappan & Gawiser 2007, Fig. 1*h*). In the SDSS *M-Z* relation, where stellar mass is in log space, a factor of ~1.5 would result in a shift of ~0.17 dex. We consider this shift when comparing the NFGS and SDSS *M-Z* relations (§ 8).

## 4. METALLICITY ESTIMATES

Metallicity calibrations have been developed over more than three decades from either theoretical models, empirical calibrations, or a combination of the two. We apply 10 different metallicity calibrations to the SDSS to investigate the impact of the metallicity calibration on the *M-Z* relation. We divide the 10 calibrations into four classes: (1) direct, (2) empirical, (3) theoretical, and (4) calibrations that are a combination of empirical and theoretical methods. The empirical, theoretical, and combined calibrations all use ratios of strong emission lines and are often referred to collectively as "strong-line methods" to distinguish them from the "direct" method based on the weak [O III] $\lambda$4363 auroral line.

In this paper we investigate the direct method, five theoretical calibrations, three empirical calibrations, and one "combined" calibration. We briefly discuss each class of calibration below. The equations, assumptions, and detailed description of each method that we use are provided in Appendix A and summarized in Table 1.

### 4.1. *Direct Metallicities*

The most direct method for determining metallicities is to measure the ratio of the [O III] $\lambda$4363 auroral line to a lower excitation line such as [O III] $\lambda$5007. This ratio provides an estimate of the electron temperature of the gas, assuming a classical H II region model. The electron temperature is then converted into a metallicity, after correcting for unseen stages of ionization. This method is sometimes referred to as the ionization correction factor (ICF), or more commonly the "direct" method or the "$T_e$" method. Determining metallicity from the auroral [O III] $\lambda$4363 line is subject to a number of caveats:

1. The [O III] $\lambda$4363 line is very weak, even in metal-poor environments, and cannot be observed in higher metallicity

[2] The error quoted on the covering fraction is the standard error of the mean.

TABLE 1
Comparison of the 10 Metallicity Calibrations

| Number | ID | Emission Lines | Calibration Class | References |
|---|---|---|---|---|
| 1..... | T04[a] | [O II], H$\beta$, [O III], H$\alpha$, [N II], [S II] | Theoretical | T04 |
| 2..... | Z94 | $R_{23}$ | Theoretical | Z94 |
| 3..... | KK04 | $R_{23}$, [O III]/[O II] | Theoretical | KK04 |
| 4..... | KD02 | [N II]/[O II], $R_{23}$, [O III]/[O II] | Theoretical | KD02 |
| 5..... | M91 | $R_{23}$, [O III]/[O II] | Theoretical | M91 |
| 6..... | D02 | [N II]/H$\alpha$ | Combined | D02 |
| 7..... | PP04 | [N II]/Ha, [O III]/H$\beta$ | Empirical | PP04 |
| 8..... | PP04 | [N II]/Ha | Empirical | PP04 |
| 9..... | P01, P05 | $R_{23}$, [O III]/[O II] | Empirical | P01; P05 |
| 10..... | $T_e$ | [O III] $\lambda$4363, [O III] $\lambda\lambda$4959, 5007 | Direct | Aller (1984); Stasińska (2005); Izotov et al. (2006a) |

[a] The T04 method uses a statistical technique to calculate the probability distribution of an object having a particular metallicity based on model fits to the [O II], H$\beta$, [O III], H$\alpha$, [N II], and [S II] emission lines.

galaxies without very sensitive, high-S/N spectra (e.g., Garnett et al. 2004b).

2. Temperature fluctuations or gradients within high-metallicity H II regions may cause electron temperature metallicities to be underestimated by as much as $\sim$0.4 dex (Stasińska 2002, 2005; Bresolin 2006). In the presence of temperature fluctuations or gradients, [O III] is emitted predominantly in high-temperature zones where $O^{++}$ is present only in small amounts. In this scenario, the high electron temperatures estimated from the [O III] $\lambda$4363 line are not representative of the true electron temperature in the H II region, leading to systematically low metallicity estimates (see reviews by Stasińska 2005; Bresolin 2006).

3. The $T_e$ method may underestimate global spectra of galaxies. Kobulnicky & Zaritsky (1999) found that for low-metallicity galaxies, the $T_e$ method systematically underestimates the global oxygen abundance of ensembles of H II regions.

High-S/N spectra can overcome the weakness of the [O III] $\lambda$4363 line, and alternative auroral lines such as the [N II] $\lambda$5755, [S III] $\lambda$6312, and [O II] $\lambda$7325 lines are observable at higher metallicities than the [O III] $\lambda$4363 line (Kennicutt et al. 2003; Bresolin et al. 2004; Garnett et al. 2004b). The theoretical investigation by Stasińska (2005) predicts that these lines can provide robust metallicities up to roughly solar [$12 + \log(\mathrm{O/H}) = 8.7$; Allende Prieto et al. 2001], but they may underestimate the abundance at metallicities above solar if temperature fluctuations or gradients exist in the nebula.

### 4.2. *Empirical Metallicity Calibrations*

Because [O III] $\lambda$4363 is weak, empirical metallicity calibrations were developed by fitting the relationship between direct $T_e$ metallicities and strong-line ratios for H II regions. Typical calibrations are based on the optical line ratios [N II] $\lambda$6584/H$\alpha$ (PP04), ([O II]/H$\beta$)/([N II]/H$\alpha$) (PP04), or the "$R_{23}$" ratio [([O II] $\lambda$3727 + [O III] $\lambda\lambda$4959, 5007)/H$\beta$; P01; P05; Liang et al. 2007; Yin et al. 2007b]. PP04 fit the observed relationships between [N II]/H$\alpha$, [O II]/H$\beta$/[N II]/H$\alpha$, and metallicity for a sample of 137 H II regions. We refer to the PP04 methods as empirical because 97% of their sample has $T_e$ metallicities.

P01 derived an empirical calibration for $R_{23}$ based on $T_e$ metallicities for a sample of H II regions. This calibration has been updated by P05 using a larger sample of H II regions.

We refer to strong-line metallicity calibrations that have been calibrated empirically from $T_e$ metallicities in H II regions as "empirical methods." In this paper we apply the commonly used empirical calibrations from P01 (revised in P05) and PP04. These calibrations are described in detail in Appendix A and summarized in Table 1. These empirical calibrations are subject to the same caveats as the $T_e$ method described above.

### 4.3. *Theoretical Metallicity Calibrations*

The lack of electron temperature measurements at high metallicity led to the development of theoretical metallicity calibrations of strong-line ratios using photoionization models. These theoretical calibrations are commonly and confusingly referred to as "empirical methods." The use of photoionization models to derive metallicity calibrations is purely theoretical, and the use of the term "empirical" is a misnomer. We refer to photoionization model–based calibrations as "theoretical methods." We refer to all calibrations that are based on strong-line ratios (i.e., including empirical and theoretical methods, but excluding the $T_e$ method) as "strong-line" methods.

Current state-of-the-art photoionization models such as MAPPINGS (Sutherland & Dopita 1993; Groves et al. 2004, 2006) and Cloudy (Ferland et al. 1998) calculate the thermal balance at steps through a dusty spherical or plane-parallel nebula. The ionizing radiation field is usually derived from detailed stellar population synthesis models such as Starburst99 (Leitherer et al. 1999). The combination of population synthesis plus photoionization models allows one to predict the theoretical emission-line ratios produced at various input metallicities.

Photoionization models overcome the temperature gradient problems that may affect $T_e$ calibrations at high metallicities because photoionization models include detailed calculations of the temperature structure of the nebula. However, photoionization models have their own unique set of problems:

1. Photoionization models are limited to spherical or plane-parallel geometries.
2. The depletion of metals out of the gas phase and onto dust grains is not well constrained observationally.
3. The density distribution of dust and gas may be clumpy. This effect is not taken into account with current photoionization models.

Because of these problems, discrepancies of up to $\sim$0.2 dex exist among the various strong-line calibrations based on photoionization models (e.g., KD02; KK04 and references therein). Systematic errors introduced by modeling inaccuracies are usually estimated to be $\sim$0.1–0.15 dex (McGaugh 1991, hereafter M91; KD02). These error estimates are calculated by generating large grids of models that cover as many H II region scenarios as possible, including varying star formation histories, stellar atmosphere models, electron densities, and geometries. Differences

between the model assumptions and the true H II region ensemble that is observed in a galaxy spectrum are likely to be systematic, affecting all derived metallicities in a similar manner.

Since systematic errors affect all of the direct, empirical, and theoretical methods for deriving metallicities in high-metallicity [$12 + \log(\mathrm{O/H}) > 8.6$] environments, we do not know which method (if any) produces the *true* metallicity of an object. Fortunately, because the errors introduced are likely to be systematic, relative metallicities between galaxies are probably reliable, as long as the same metallicity calibration is used. We test this hypothesis in § 9.

Many theoretical calibrations have been developed to convert metallicity-sensitive emission-line ratios into metallicity estimates. Commonly used line ratios include [N II] $\lambda$6584/[O II] $\lambda$3727 (KD02) and ([O II] $\lambda$3727 + [O III] $\lambda\lambda$4959, 5007)/H$\beta$ (Pagel et al. 1979; M91; Z94; KK04). In addition to the use of specific line ratios to derive metallicities, theoretical models can be used to simultaneously fit all observed optical emission lines to derive a metallicity probability distribution, as in T04. T04 estimated the metallicity for SDSS star-forming galaxies statistically based on theoretical model fits to the strong emission lines [O II], H$\beta$, [O III], H$\alpha$, [N II], and [S II].

In this paper we apply the M91, Z94, KK04, KD02, and T04 theoretical calibrations, described in detail in Appendix A. Many empirical and theoretical metallicity calibrations rely on the double-valued ([O II] $\lambda$3727 + [O III] $\lambda\lambda$4959, 5007)/H$\beta$ line ratio, known as $R_{23}$. In § A1 we derive the [N II]/H$\alpha$ and [N II]/[O II] values that can be used to break the $R_{23}$ degeneracy in a model-independent way.

### 4.4. *Combined Calibration*

Some metallicity calibrations are based on fits to the relationship between strong-line ratios and H II region metallicities, where the H II region metallicities are derived from a combination of theoretical, empirical, and/or the direct $T_e$ method. For example, the D02 calibration is based on a fit to the relationship between the $T_e$ metallicities and the [N II]/H$\alpha$ line ratio for ~155 H II regions. Of these 155 H II regions, ~100 have metallicities derived using the $T_e$ method, and 55 have metallicities estimated using either the theoretical M91 $R_{23}$ method or an empirical method proposed by Díaz & Pérez-Montero (2000) based on the sulfur lines. We refer to calibrations that are based on a combination of methods as "combined" calibrations. In this paper we apply the D02 combined calibration (described in Appendix A).

## 5. THE *M-Z* RELATION: METALLICITY CALIBRATIONS

In Figure 1 we show the *M-Z* relation obtained using each of the 10 metallicity calibrations. There are insufficient galaxies in the SDSS with [O III] $\lambda$4363 detections to determine an *M-Z* relation using the $T_e$ metallicities. For the strong-line methods (i.e., all methods except the direct $T_e$ method), the red line shows the robust best-fitting third-order polynomial to the data. The blue circles give the median metallicity within masses of $\log M = 0.2\ M_\odot$, centered at $\log M = 8.6, 8.8, \ldots, 11\ M_\odot$. Both methods of characterizing the shape of the *M-Z* relations produce similar results. The parameters of the best-fit polynomials and the rms residuals of the fit are given in Table 2.

The different strong-line calibrations produce *M-Z* relations with different shapes, *y*-axis offsets, and scatter. T04 interpret the flattening in the *M-Z* relation above stellar masses $\log M > 10.5\ M_\odot$ in terms of efficient galactic-scale winds that remove metals from the galaxies with masses below $\log M < 10.5\ M_\odot$. A similar flattening is observed for the majority of the theoretical

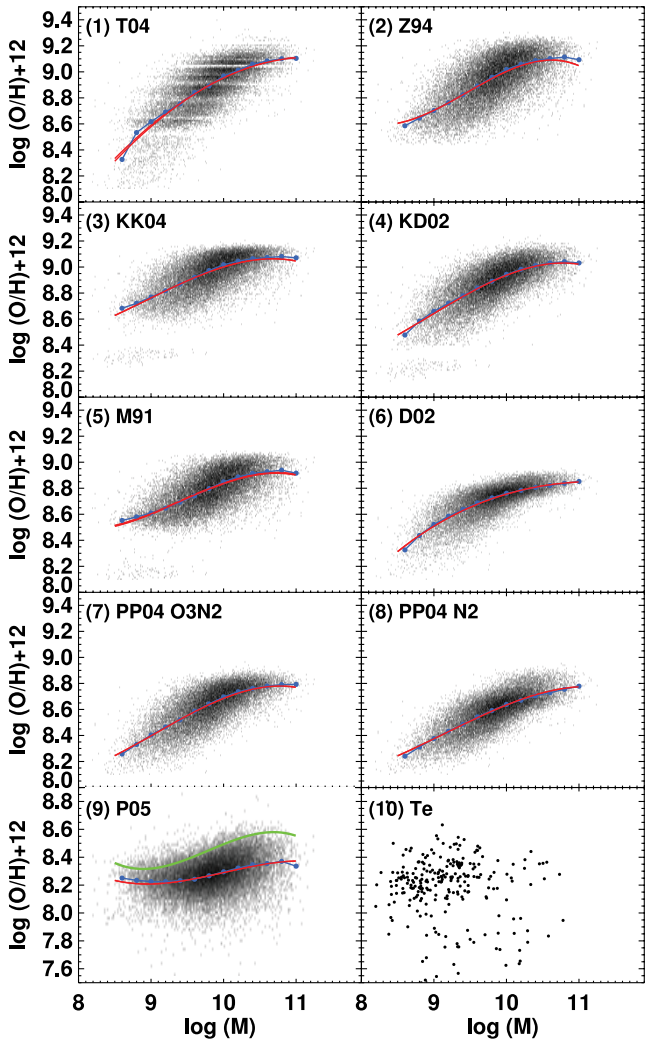


FIG. 1.—*M-Z* relation using the 10 different metallicity calibrations listed in Table 1. The red line shows the robust best-fitting third-order polynomial to the data. The blue circles give the median metallicity within stellar mass bins of $\Delta\log(M/M_\odot) = 0.2$, centered at $\log(M/M_\odot) = 8.6, 8.8, \ldots, 11$. We use the updated calibration of P05 in panel (9). The original P01 calibration is shown as a solid green line in panel (9).

techniques. However, the *M-Z* relations calculated using metallicity calibrations based on [N II]/H$\alpha$ (D02 and PP04 N2) flatten at lower stellar masses $\log M \sim 10$ because the [N II]/H$\alpha$ line ratio becomes insensitive to metallicities for $\log([\mathrm{N\ II}]/\mathrm{H}\alpha) \gtrsim -1$ (or $12 + \log(\mathrm{O/H}) \gtrsim 8.8$ in the D02 or PP04 [N II]/H$\alpha$–based metallicity scale). The [N II]/H$\alpha$ calibrations cannot give metallicity estimates above $12 + \log(\mathrm{O/H}) \gtrsim 8.8$, even if the true metallicity is higher than $12 + \log(\mathrm{O/H}) > 8.8$.

The P05 empirical method is relatively flat for all stellar masses; between $8.5 \leq \log(M/M_\odot) \leq 11$, the metallicity rises only ~0.2 dex on average. The majority of the H II regions used by P05 have $T_e$ metallicities that are based on the [O III] $\lambda$4363 line. Because the [O III] $\lambda$4363 line may be insensitive to (or saturate at) a metallicity $12 + \log(\mathrm{O/H}) \sim 8.6$, the P05 calibration may give a weak *M-Z* relation for the SDSS. Interestingly, the original P01 calibration (green line in panel [9] of Fig. 1) gives a steeper *M-Z* relation than the updated calibration (P05; *red and blue lines*). The updated P05 relation also produces lower absolute metallicities by ~0.2 dex compared with the original P01 method, as pointed out by Yin et al. (2007b) in their comparison between P01, P05, and T04 metallicities. This change may be

TABLE 2
ROBUST FITS TO THE *M-Z* RELATIONS FOR THE NINE STRONG-LINE METALLICITY CALIBRATIONS

| ID | *a* | *b* | *c* | *d* | rms Residuals |
|---|---|---|---|---|---|
| T04 | −0.694114 | 1.30207 | 0.00271531 | −0.00364112 | 0.12 |
| Z94 | 72.0142 | −20.6826 | 2.22124 | −0.0783089 | 0.13 |
| KK04 | 27.7911 | −6.94493 | 0.808097 | −0.0301508 | 0.10 |
| KD02 | 28.0974 | −7.23631 | 0.850344 | −0.0318315 | 0.10 |
| M91 | 45.5323 | −12.2469 | 1.32882 | −0.0471074 | 0.11 |
| D02 | −8.71120 | 4.15003 | −0.322156 | 0.00818179 | 0.08 |
| PP04 O3N2 | 32.1488 | −8.51258 | 0.976384 | −0.0359763 | 0.10 |
| PP04 N2 | 23.9049 | −5.62784 | 0.645142 | −0.0235065 | 0.09 |
| P01 | 91.6457 | −25.9355 | 2.67172 | −0.0909689 | 0.12 |
| P05 | 41.9463 | −10.3253 | 1.04371 | −0.0347747 | 0.13 |

NOTE.—Robust fits are of the form $y = a + bx + bx^2 + bx^3$, where $y = \log(\mathrm{O/H}) + 12$ and $x = \log M$, where $M$ is the stellar mass in solar units.

caused by the different H II region abundance sets that were used to calibrate the original P01 method and the updated version in P05.

The direct $T_e$ method is available for only 546/27,730 (2%) of the galaxies in our SDSS sample. The [O III] $\lambda$4363 line is weak and is usually only observed in metal-poor galaxies. The SDSS catalog contains very few metal-poor galaxies because they are intrinsically rare, compact, and faint (e.g., Terlevich et al. 1991; Masegosa et al. 1994; van Zee 2000). Panel (10) of Figure 1 shows that a total of 477 $T_e$ metallicities is insufficient to obtain a clear *M-Z* relation. Because we are unable to fit an *M-Z* relation using $T_e$ metallicities, we do not consider the $T_e$ method further in this work.

The scatter in the *M-Z* relation is large for all metallicity calibrations; the rms residual about the line of best fit is 0.08–0.13. The cause of the scatter in the *M-Z* relation is unknown. Our comparison between the different metallicity calibrations shows that differing the ionization parameter among galaxies does not cause or contribute to the scatter. The ionization parameter is explicitly calculated and taken into account in some metallicity diagnostics (KD02; KK04; M91), but we do not see a reduction in scatter for these methods. A full investigation into the scatter in the *M-Z* relation will be presented in S. L. Ellison et al. (2008, in preparation).

We directly compare the best-fit *M-Z* curves for the nine strong-line calibrations in Figure 2, including both P01 and P05. The top panel shows the rms scatter in metallicity about the mean in mass bins of width $\Delta\log(M/M_\odot) = 0.2$. The major difference between the *M-Z* curves is their position along the *y*-axis. The curves with the largest *y*-intercept are all photoionization model based (KK04; Z94; KD02; T04; M91). Among these photoionization model metallicities, the agreement is ~0.2 dex. This agreement is within the margin of error typically cited for these calibrations (~0.1–0.15 dex for each calibration). Some calibrations consistently agree to within 0.1 dex (e.g., KK04 and Z94; KD02 and M91). Comparisons between metallicities calculated using these consistent methods, such as KD02 and M91, are likely to be reliable to within 0.1 dex. However, comparisons between methods that show large disagreement (such as KK04 and P05) will be contaminated by the large systematic discrepancy between the calibrations.

The lowest curves in Figure 2 are the *M-Z* relations derived using the empirical methods (i.e., P01, P05, and the two PP04 methods). These empirical methods are calibrated predominantly via fits of the relationship between strong-line ratios and H II region $T_e$ metallicities. There is considerable variation among the *y*-intercept of these $T_e$-based *M-Z* relations; the P05 method gives metallicities that are ~0.4 dex below the PP04 methods at the highest masses, despite the fact that both methods are predominantly based on H II regions with $T_e$ metallicities. At the lowest stellar masses, this difference disappears. The difference between the empirical methods may be attributed to the different H II region samples used to derive the calibrations. At the highest metallicities, the PP04 methods utilize four H II regions with detailed

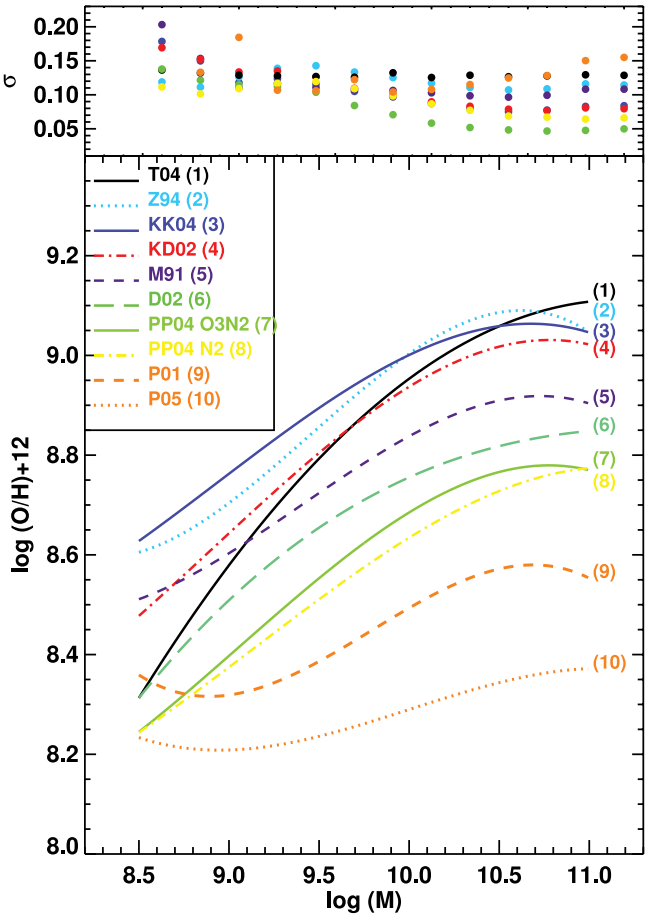


FIG. 2.—Robust best-fit *M-Z* relations calculated using the different metallicity calibrations listed in Table 1, except the $T_e$ method. The top panel shows the rms scatter in metallicity about the best-fit relation for each calibration in 0.1 dex bins of stellar mass. The *y*-axis offset, shape, and scatter of the *M-Z* relation differ substantially, depending on which metallicity calibration is used.

theoretical metallicities. These detailed theoretical metallicities may overcome the saturation at $12 + \log(\mathrm{O/H}) \sim 8.6$ suffered by [O III] $\lambda4363$ $T_e$ metallicities. The P05 calibration includes some H II regions with metallicities estimated with the alternative auroral [N II] $\lambda5755$ line from Kennicutt et al. (2003). The inclusion of these [N II] $\lambda5755$ metallicities may overcome the [O III] $\lambda4363$ saturation problem. However, Stasińska (2005) suggests that the use of the [N II] $\lambda5755$ line in dusty nebulae will still cause $T_e$ metallicities to be underestimated when the true metallicity is above solar. Our SDSS sample has a mean extinction of $E(B-V) \sim 0.3$, or $A_V \sim 1$. The extinction is a strong function of stellar mass; for the largest stellar masses ($M > 10^{10.5}\ M_\odot$), the mean extinction is large, $E(B-V) \sim 0.5$, or $A_V \sim 1.6$. Clearly, dust is important in SDSS galaxies, particularly at the highest stellar masses where the largest discrepancies exist between the theoretical methods and the P05 $T_e$ methods.

In addition to the large difference in $y$-intercept between the different metallicity calibrations, Figure 2 shows that the slope and turnover of the *M-Z* relation depend on which calibration is used. Therefore, it is essential to compare *M-Z* relations that have been calculated using the same metallicity calibration. In the following section we derive conversions that can be used to convert metallicities from one calibration into another.

## 6. METALLICITY CALIBRATION CONVERSIONS

Comparisons between *M-Z* relations for galaxies in different redshift ranges are nontrivial. Different suites of emission lines are available at different redshifts, necessitating the use of different metallicity calibrations. Because of the strong discrepancy in absolute metallicities between different calibrations, the application of different calibrations for galaxies at different redshifts may mimic or hide evolution in the *M-Z* relation with redshift, depending on which calibrations are used. Because the metallicity discrepancies are systematic, we can fit the relationship between the different metallicity calibrations in order to remove the systematic discrepancies and obtain comparable metallicity measurements for different redshift intervals.

We calculate conversion relations between the strong-line metallicity calibrations by plotting each calibration against the remaining eight calibrations and fitting the resulting metallicity-metallicity distribution with a robust polynomial fit. We refer to these metallicity-metallicity plots as *Z-Z* plots. Rows 1–3 of Figure 3 give six representative examples of SDSS *Z-Z* plots for the strong-line calibrations. The *Z-Z* plots between all nine strong-line calibrations for various S/N cuts are available online.[3] The blue dashed 1 : 1 line shows where the *Z-Z* distribution would lie if the two calibrations agree. The robust best-fit polynomial is shown in red, and $\rho_r$ gives the robust equivalent to the standard deviation of the fit. Small values of $\rho_r$ indicate a reliable fit to the data.

The majority of the *Z-Z* relations are close to linear and are easily fitted by a first-, second-, or third-order robust polynomial. However, the P05 calibration produces a very nonlinear relation with a large scatter when plotted against all other metallicity calibrations. These nonlinear relations are not easily fitted even with a robust third-order polynomial, and we cannot provide conversions that will reliably convert to/from the P05 method. For comparison, the bottom row of Figure 3 shows the same plots calculated with the original P01 calibration. Although the scatter is less severe in these plots, the relations between P01 and other diagnostics remain nonlinear and are not easily fitted with a robust third-order polynomial.

[3] See http://www.ifa.hawaii.edu/~kewley/Metallicity.

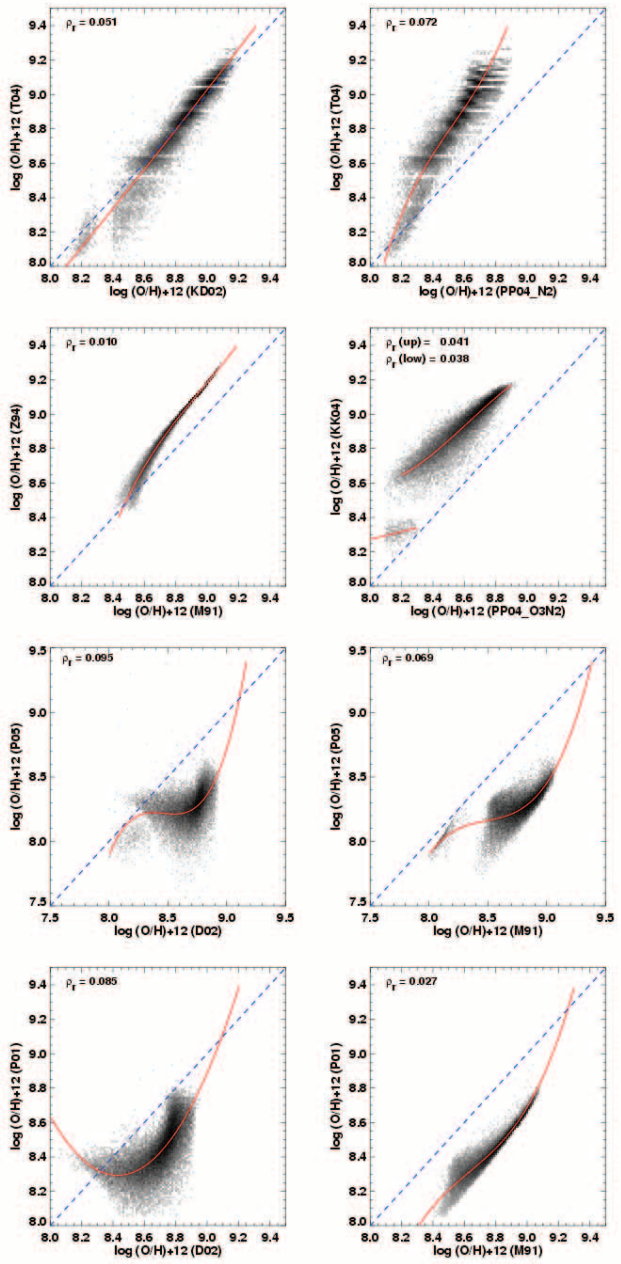


FIG. 3.—Examples of the relationship between different metallicity calibrations. The robust second-order polynomial of best fit is shown as a red solid line. The 1 : 1 lines (*blue dashed lines*) show where the metallicities would lie if the calibrations agree. The robust equivalent to the standard deviation of the fit ($\rho_r$) is shown for each plot. This figure illustrates the typical variation in scatter and shape between different metallicity calibrations. Figures showing the relations between all nine strong-line metallicity calibrations are available online (see footnote 3).

For all other diagnostics, the metallicities or metallicity relations can be converted into any other calibration scheme, using

$$y = a + bx + cx^2 + dx^3, \quad (1)$$

where $y$ is the "base" or final metallicity in $12 + \log(\mathrm{O/H})$ units, $a$–$d$ are the third-order robust fit coefficients given in Table 3, and $x$ is the original metallicity to be converted [in $12 + \log(\mathrm{O/H})$ units]. For *Z-Z* relations where a second-order polynomial produces a lower $\rho_r$ than a third-order polynomial fit, $d$ is zero.

The conversion coefficients given in Table 3 are based on the fit order that produces the lowest $\rho_r$ value in our sample. Some

TABLE 3

METALLICITY CALIBRATION CONVERSION CONSTANTS

| ID ($y$) | KK04 ($x$) | Z94 ($x$) | M91 ($x$) | KD02 ($x$) | T04 ($x$) | D02 ($x$) | PP04 O3N2 ($x$) | PP04 N2 ($x$) |
|---|---|---|---|---|---|---|---|---|
| | | | | KK04 | | | | |
| $x$-range[a] | ... | 8.4–9.3 | 8.4–9.1; 8.0–8.25 | 8.4–9.2; 8.05–8.3 | 8.3–9.2; 8.05–8.4 | 8.2–8.9; 8.05–8.4 | 8.2–8.9; 8.05–8.3 | 8.2–8.9; 8.05–8.3 |
| Branch[b] | ... | ... | up; low | up; low | up; low | up; low | up; low | up; low |
| $a$ | ... | 3 48.1710 | −355.2968; 2.0021 | 1149.479; 1.0944 | −162.1918; 5.0521 | −1.7278; 6.5483 | 389.1568; 6.5339 | 211.1405; 5.2218 |
| $b$ | ... | −117.65370 | 114.8835; 0.77696 | −389.9349; 0.87842 | 57.57935; 0.39887 | 1.52612; 0.21508 | −133.79070; 0.21761 | −81.11275; 0.37813 |
| $c$ | ... | 13.502640 | −12.09838 | 44.33080 | −6.533486 | −0.034389 | 15.59350 | 10.577470 |
| $d$ | ... | −0.5130281 | 0.4258375 | −1.675994 | 0.249956 | ... | −0.6020232 | −0.4510567 |
| $\rho_r$ | ... | 0.003 | 0.007; 0.007 | 0.031; 0.004 | 0.048; 0.029 | 0.065; 0.039 | 0.041; 0.041 | 0.064; 0.038 |
| | | | | Z94 | | | | |
| $x$-range[a] | 8.55–9.2 | ... | 8.4–9.1 | 8.4–9.2 | 8.4–9.2 | 8.05–8.9 | 8.05–8.9 | 8.05–8.8 |
| $a$ | −1112.0910 | ... | −868.280 | 1086.903 | 11.2595 | 63.6386 | 230.9335 | 40.5515 |
| $b$ | 379.11370 | ... | 291.6262 | −366.5700 | −1.47641 | −13.87785 | −76.73906 | −8.67461 |
| $c$ | −42.880040 | ... | −32.42779 | 41.41521 | 0.136681 | 0.872216 | 8.711059 | 0.581691 |
| $d$ | 1.6218750 | ... | 1.206416 | −1.554630 | ... | ... | −0.3244087 | ... |
| $\rho_r$ | 0.005 | ... | 0.010 | 0.040 | 0.056 | 0.081 | 0.052 | 0.076 |
| | | | | M91 | | | | |
| $x$-range[a] | 8.25–9.15 | 8.4–9.2 | ... | 8.4–9.2; 8.1–8.4 | 8.2–9.2; 8.05–8.4 | 8.2–8.9; 8.05–8.4 | 8.2–8.9; 8.05–8.4 | 8.2–8.8; 8.05–8.3 |
| Branch[b] | ... | ... | ... | up; low | up; low | up; low | 8.2–8.9; 8.05–8.4 | up; low |
| $a$ | −641.2458 | 393.9855 | ... | 890.1334; −1.0907 | 404.1716; 3.0825 | 85.2839; 4.7927 | 267.3936; 2.4196 | 87.3710; 0.7641 |
| $b$ | 226.42050 | −127.86040 | ... | −295.90760; 1.12114 | −131.53250; 0.61779 | −18.63342; 0.40796 | −85.20014; 0.70167 | −19.39959; 0.90362 |
| $c$ | −26.374200 | 14.050330 | ... | 33.004210 | 14.491750 | 1.130870 | 9.219665 | 1.193544 |
| $d$ | 1.0268860 | −0.5109532 | ... | −1.2227730 | −0.5285842 | ... | −0.3267103 | ... |
| $\rho_r$ | 0.008 | 0.008 | ... | 0.034; 0.004 | 0.047; 0.044 | 0.071; 0.059 | 0.048; 0.076 | 0.064; 0.070 |
| | | | | KD02 | | | | |
| $x$-range[a] | 8.2–9.2 | 8.4–9.2 | 8.5–9.1; 8.05–8.3 | ... | 8.2–9.2; 8.05–8.4 | 8.2–8.9; 8.05–8.4 | 8.2–8.9; 8.05–8.3 | 8.2–8.9; 8.05–8.3 |
| Branch[b] | ... | ... | up; low | ... | up; low | up; low | up; low | up; low |
| $a$ | 75.5327 | −476.8939 | −2127.7470; 1.0007 | ... | 387.2871; 4.1582 | 47.3054; 5.9875 | 159.0567; 5.8961 | 1094.5410; 4.5323 |
| $b$ | −23.64323 | 160.45270 | 720.35980; 0.88853 | ... | −129.69190; 0.49751 | −10.06952; 0.27338 | −54.18511; 0.28562 | −388.67530; 0.45232 |
| $c$ | 2.658484 | −17.752170 | −81.051380 | ... | 14.718030 | 0.649502 | 6.395364 | 46.233760 |
| $d$ | −0.0948578 | 0.6579900 | 3.0435570 | ... | −0.5531547 | ... | −0.2471693 | −1.8276270 |
| $\rho_r$ | 0.038 | 0.036 | 0.038; 0.003 | ... | 0.041; 0.039 | 0.048; 0.055 | 0.047; 0.059 | 0.047; 0.054 |
| | | | | T04 | | | | |
| $x$-range[a] | 8.6–9.15; 8.2–8.4 | 8.4–9.2 | 8.6–9.1; 8.05–8.4 | 8.1–9.2 | ... | 8.05–8.9 | 8.05–8.9 | 8.05–8.9 |
| Branch[b] | up; low | ... | up; low | ... | ... | ... | ... | ... |
| $a$ | −461.2352; −4.5710 | −472.8841 | −69.7024; −1.0200 | 1.3782 | ... | 193.9000 | −738.1193 | −1661.9380 |
| $b$ | 158.44840; 1.53261 | 158.20310 | 16.68313; 1.13063 | 0.52591 | ... | −64.87895 | 258.96730 | 585.17650 |
| $c$ | −17.946070 | −17.414190 | −0.880678 | 0.036003 | ... | 7.411102 | −30.057050 | −68.471750 |
| $d$ | 0.6828170 | 0.6427315 | ... | ... | ... | −0.2756653 | 1.1679370 | 2.6766690 |
| $\rho_r$ | 0.060; 0.060 | 0.062 | 0.062; 0.063 | 0.051 | ... | 0.072 | 0.058 | 0.072 |

TABLE 3 — *Continued*

| ID ($y$) | KK04 ($x$) | Z94 ($x$) | M91 ($x$) | KD02 ($x$) | T04 ($x$) | D02 ($x$) | PP04 O3N2 ($x$) | PP04 N2 ($x$) |
|---|---|---|---|---|---|---|---|---|
| | | | | D02 | | | | |
| $x$-range[a] | 8.2–9.2 | 8.4–9.3 | 8.5–9.1; 8.0–8.4 | 8.05–9.2 | 8.05–9.2 | ... | 8.05–8.9 | 8.05–8.9 |
| Branch[b] | ... | ... | up; low | ... | ... | ... | ... | ... |
| $a$ | 1202.5280 | −114.3143 | −121.3958; −1.0361 | 680.5167 | 253.0031 | ... | −1.3992 | −629.0499 |
| $b$ | −412.30820 | 32.79523 | 28.86410; 1.13468 | −235.27350 | −87.03697 | ... | −5.32702 | 215.37940 |
| $c$ | 47.332730 | −2.782591 | −1.599613 | 27.345830 | 10.241880 | ... | 1.562757 | −24.305910 |
| $d$ | −1.8065160 | 0.0731175 | ... | −1.0552390 | −0.3984731 | ... | −0.0938063 | 0.9168766 |
| $\rho_r$ | 0.058 | 0.056 | 0.061; 0.093 | 0.038 | 0.044 | ... | 0.033 | 0.000 |
| | | | | PP04 (O3N2) | | | | |
| $x$-range[a] | 8.2–9.2 | 8.4–9.3 | 8.5–9.1; 8.05–8.4 | 8.1–9.2 | 8.05–9.2 | 8.05–8.9 | ... | 8.05–8.8 |
| Branch[b] | ... | ... | up; low | ... | ... | ... | ... | ... |
| $a$ | 631.2766 | 52.2389 | −65.0991; 2.1063 | 664.8453 | 230.7820 | 36.6598 | ... | −8.0069 |
| $b$ | −210.02090 | −18.67559 | 15.74995; 0.74427 | −225.75330 | −75.79752 | −7.64786 | ... | 2.74353 |
| $c$ | 23.483050 | 2.447698 | −0.837514 | 25.768880 | 8.526986 | 0.508480 | ... | −0.093680 |
| $d$ | −0.8704286 | −0.1011578 | ... | −0.9761368 | −0.3162894 | ... | ... | ... |
| $\rho_r$ | 0.050 | 0.047 | 0.056; 0.073 | 0.047 | 0.046 | 0.045 | ... | 0.038 |
| | | | | PP04 (N2) | | | | |
| $x$-range[a] | 8.2–9.2 | 8.4–9.3 | 8.5–9.1; 8.05–8.4 | 8.05–9.2 | 8.05–9.2 | 8.05–8.9 | 8.05–8.9 | ... |
| Branch[b] | ... | ... | up; low | ... | ... | ... | ... | ... |
| $a$ | 916.7484 | 656.5128 | 1334.9130; 3.1447 | 569.4927 | 319.7570 | −444.7831 | 512.7575 | ... |
| $b$ | −309.54480 | −224.11240 | −464.86390; 0.61788 | −192.51820 | −107.13160 | 165.42600 | −180.47540 | ... |
| $c$ | 35.051680 | 25.734220 | 54.166750 | 21.918360 | 12.208670 | −20.202000 | 21.415880 | ... |
| $d$ | −1.3188000 | −0.9812624 | −2.0986640 | −0.8278840 | −0.4606539 | 0.8249386 | −0.8427312 | ... |
| $\rho_r$ | 0.068 | 0.065 | 0.071; 0.050 | 0.045 | 0.051 | 8.557E−6 | 0.042 | ... |

NOTE.—The conversion constants convert metallicities from the calibrations given in row 1 ($x$) into a metallicity that is consistent with the calibration given in the first column ($y$), using $y = a + bx + cx^2 + dx^3$.

[a] The range over which a metallicity using a calibration given in row 1 ($x$) can be converted into a metallicity that is consistent with the calibration given in the first column ($y$).

[b] Some conversions are different, depending on whether the input metallicity ($x$) is on the upper or lower branch (up; low). In some regimes, both the upper and lower branch conversion equations are valid. In these cases, additional information such as an [N II]/[O II] or [N II]/H$\alpha$ ratio is needed to distinguish between the upper and lower $R_{23}$ branches. A worked example for this case is given in Appendix B.

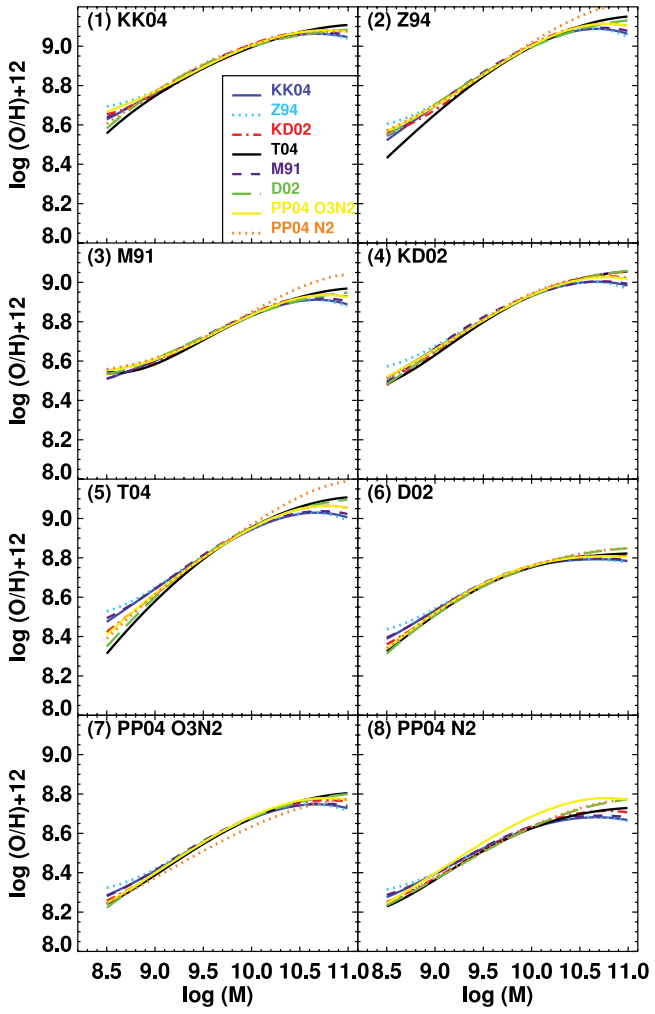


FIG. 4.—Robust best-fit *M-Z* relations calculated using the eight different metallicity calibrations listed in Table 1, converted into the base metallicities shown using our conversions from Table 3.

$R_{23}$ calibrations require two fits: one second- or third-order fit for the upper $R_{23}$ branch and one linear fit for the lower branch. In these cases, the coefficients of the upper and lower branch fits are listed in the first and last columns of Table 3, respectively.

In Table 3 we give the range in $x$ over which our calibrations are valid. Our polynomial fits are only tested within these ranges and may not be suitable for converting lower or higher metallicities into another scheme outside these limits. We provide worked examples for the use of our conversions in Appendix B.

Figure 4 shows the application of our strong-line conversions to the best-fit *M-Z* relations in Figure 2, excluding P05. The calibration shown for each panel represents the base (final) calibration into which all other *M-Z* curves have been converted. The remaining discrepancy between the converted *M-Z* relation and the base *M-Z* relation is an indicator of both the scatter in our *Z-Z* plots and how well the *Z-Z* relations are fitted by a robust polynomial. In Table 4 we give the mean residual discrepancy between the converted *M-Z* relations and the base *M-Z* relation.

Our conversions reach agreement between the *M-Z* relations to within ~0.03 dex on average. The most reliable base calibrations are those with the smallest residual discrepancies. The residual discrepancies differ because some *Z-Z* relations have less scatter and/or are more easily fitted by a simple polynomial. The KK04, M91, PP04 O3N2, and KD02 methods have the smallest residual discrepancies and are therefore the most reliable base calibrations to convert other metallicities into.

TABLE 4
RESIDUAL METALLICITY DISCREPANCY

| Base ID[a] | Mean Residual Discrepancy[b] (dex) |
|---|---|
| KK04 | 0.011 |
| Z94 | 0.018 |
| M91 | 0.011 |
| KD02 | 0.014 |
| T04 | 0.034 |
| D02 | 0.034 |
| PP04 O3N2 | 0.012 |
| PP04 N2 | 0.021 |

[a] Calibration into which the other seven *M-Z* relations have been converted.
[b] Mean residual metallicity discrepancy between the seven converted *M-Z* relations and the base *M-Z* relation.

## 7. THE *M-Z* RELATION: AGN REMOVAL METHODS

The nebular emission line spectrum is sensitive to the hardness of the ionizing extreme-ultraviolet radiation. Metallicities calculated from spectra that contain a significant contribution from an AGN may be spurious because the commonly used metallicity calibrations are based on the assumption of a stellar ionizing radiation field. The standard optical diagnostic diagrams for classification were first proposed by Baldwin et al. (1981) based on the line ratios [N II]/H$\alpha$ versus [O II]/H$\beta$, [S II] versus [O II]/H$\beta$, and [O I]/H$\alpha$ versus [O II]/H$\beta$. This classification scheme was revised by Osterbrock & Pogge (1985) and Veilleux & Osterbrock (1987, hereafter VO87), who used a combination of AGN and starburst samples with photoionization models to derive a classification line on the diagnostic diagrams to separate AGNs from starburst galaxies. Subsequently, Kewley et al. (2001, hereafter K01) developed a purely theoretical "maximum starburst line" line for AGN classification using the standard diagrams. This theoretical scheme provides an improvement on the previous semiempirical classification by producing a more consistent classification line from diagram to diagram that significantly reduces the number of ambiguously classified galaxies. The "maximum starburst line" defines the maximum theoretical position on the diagnostic diagrams that can be attained by pure star formation models. According to the K01 models, galaxies lying above the maximum starburst line are dominated by AGN activity and objects lying below the line are dominated by star formation.

Although objects lying below the maximum starburst line are likely to be dominated by star formation, they may contain a small contribution from an AGN. We calculate the maximum AGN contribution that would allow a galaxy to be classified as star forming with the K01 line on all three standard diagnostic diagrams using theoretical galaxy spectra. Our AGN model is based on the $12 + \log(\mathrm{O/H}) = 8.9$ dusty radiation pressure–dominated models by Groves et al. (2004). We use a typical AGN ionization parameter of $\log U = -2$ and a power-law index of $\alpha = -1.4$. We investigate the suite of starburst models from KD02 and Dopita et al. (2000). The starburst model that allows the maximum contribution from an AGN while remaining classified as star forming is the zero-age instantaneous burst model with ionization parameter $q = 1 \times 10^7$ cm s$^{-1}$ and metallicity $12 + \log(\mathrm{O/H}) = 8.9$ (KD02; Dopita et al. 2000). The AGN contribution in this model is ~15%.

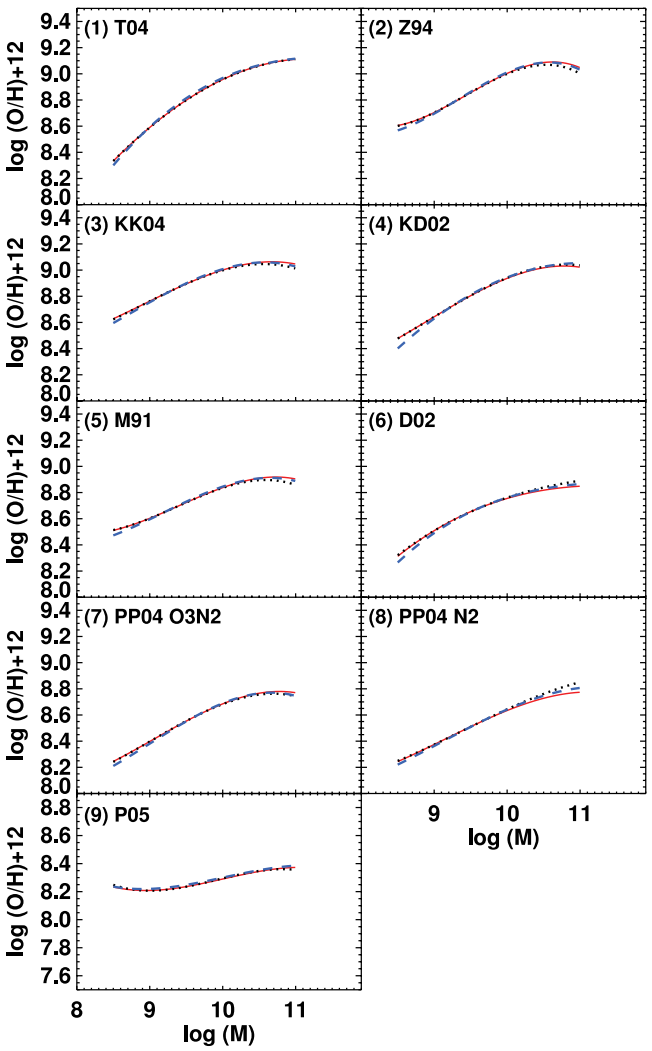


FIG. 5.—Comparison between the *M-Z* relations for three different methods of AGN removal: K06 (*red solid line*), K01 (*black dotted line*), and VO87 (*blue dashed line*). The method of AGN removal has little effect on the *M-Z* relation, except at low stellar masses, where the VO87 method gives a flatter slope.

We use this model to calculate the effect of a 15% AGN contribution to the metallicity-sensitive emission-line ratios. The AGN model contributes substantially to the [O II]/H$\beta$ line ratio but has only a minor effect on the [N II]/[O II] ratio. Therefore, the effect of an AGN contribution of 15% is small ($\leq$0.04 dex) on metallicities calculated using the [N II]/[O II] ratio (KD02), but larger (0.1–0.2 dex) on metallicities calculated with calibrations containing [O III] (e.g., M91; Z94; KK04).

Recently, K06 defined a new classification scheme based on all three diagnostic diagrams that separates pure H II region–like galaxies from H II–AGN composites, Seyferts, and galaxies dominated by LINERs. This new classification scheme includes an empirical shift applied by K03 to the K01 line for the [N II]/H$\alpha$ versus [O II]/H$\beta$ diagnostic. This shift provides a more stringent removal of objects containing AGNs, and we recommend its use for metallicities calculated using $R_{23}$.

We investigate whether the AGN classification scheme affects the shape of the *M-Z* relation in Figure 5. For each metallicity calibration, we show the *M-Z* relation for the three classification schemes of K01 (*black dotted line*), K06 (*red solid line*), and VO87 (*blue dashed line*). These three classification schemes define 89%, 84%, and 76% of our SDSS sample as star forming, respectively.

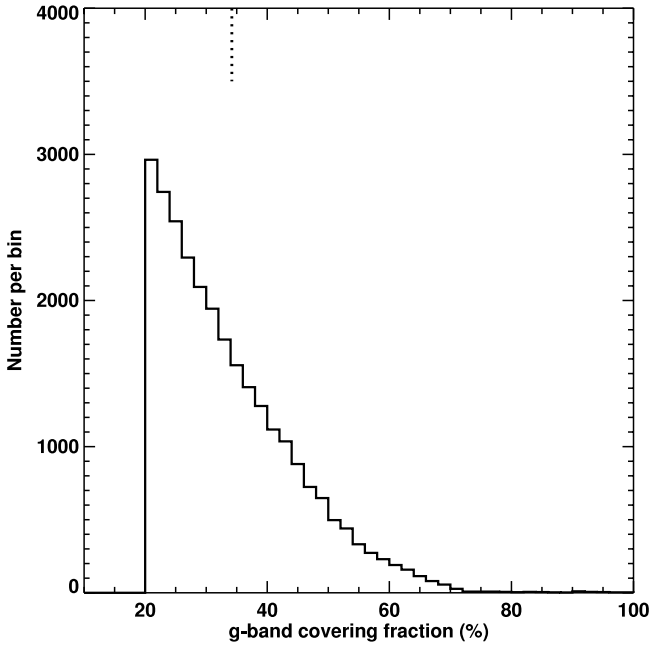


FIG. 6.—Distribution of $g'$-band fiber covering fractions in our SDSS sample. Our sample was chosen to have covering fractions >20%. The dotted line at the top indicates the median (34.2) covering fraction of our sample.

There is negligible difference (<0.05 dex) among the SDSS *M-Z* relations for the three classification schemes. We note that the contribution from an AGN may be more important for samples that contain a larger fraction of H II–AGN composite galaxies, or galaxies at high redshift where limited sets of emission lines limit the methods for AGN removal. For these cases, we recommend the use of either the KD02 [N II]/[O II] metallicity calibration [useful for log ([N II]/[O II]) $> -1.2$], the PP04 [N II]/H$\alpha$ calibration, or the D02 [N II]/H$\alpha$ calibration. None of these three calibrations depend on the AGN-sensitive [O II]/H$\beta$ line ratio.

## 8. THE *M-Z* RELATION: APERTURE EFFECTS

Our SDSS sample was selected with $g'$-band covering fractions >20% because this value is the minimum covering fraction required for metallicities to approximate the global values (Kewley et al. 2005). A covering fraction of 20% corresponds to a median redshift of $z \sim 0.04$, which is the lower redshift limit used by T04 for their SDSS *M-Z* relation work. The median $g'$-band aperture covering fraction of our sample is only ~34%, although the range of $g'$-band covering fractions is 20%–80% (Fig. 6).

Strong metallicity gradients exist in most massive late-type spirals; H II region metallicities decrease by an order of magnitude from the inner to the outer disk (for a review see, e.g., Shields 1990). These gradients may cause substantial differences between the nuclear and global metallicities. Kewley et al. (2005) investigate the effects of a fixed-size aperture on spectral properties for a large range of galaxy types and luminosity. They conclude that minimum covering fractions larger than 20% may be needed at high luminosities to avoid aperture effects. Therefore, the SDSS *M-Z* relation may be affected by the fixed-size aperture at the highest luminosities or stellar masses.

To investigate the effect of the small median SDSS covering fraction on the *M-Z* relation, in Figure 7 we compare the SDSS *M-Z* relation (*red solid line*) with the nuclear (*black dot-dashed line*) and global (*blue dashed line*) *M-Z* relations of the NFGS. We show the KD02 metallicity calibration (Figs. 7*a* and 7*c*) and the M91 calibration (Figs. 7*b* and 7*d*) for all data sets. Similar

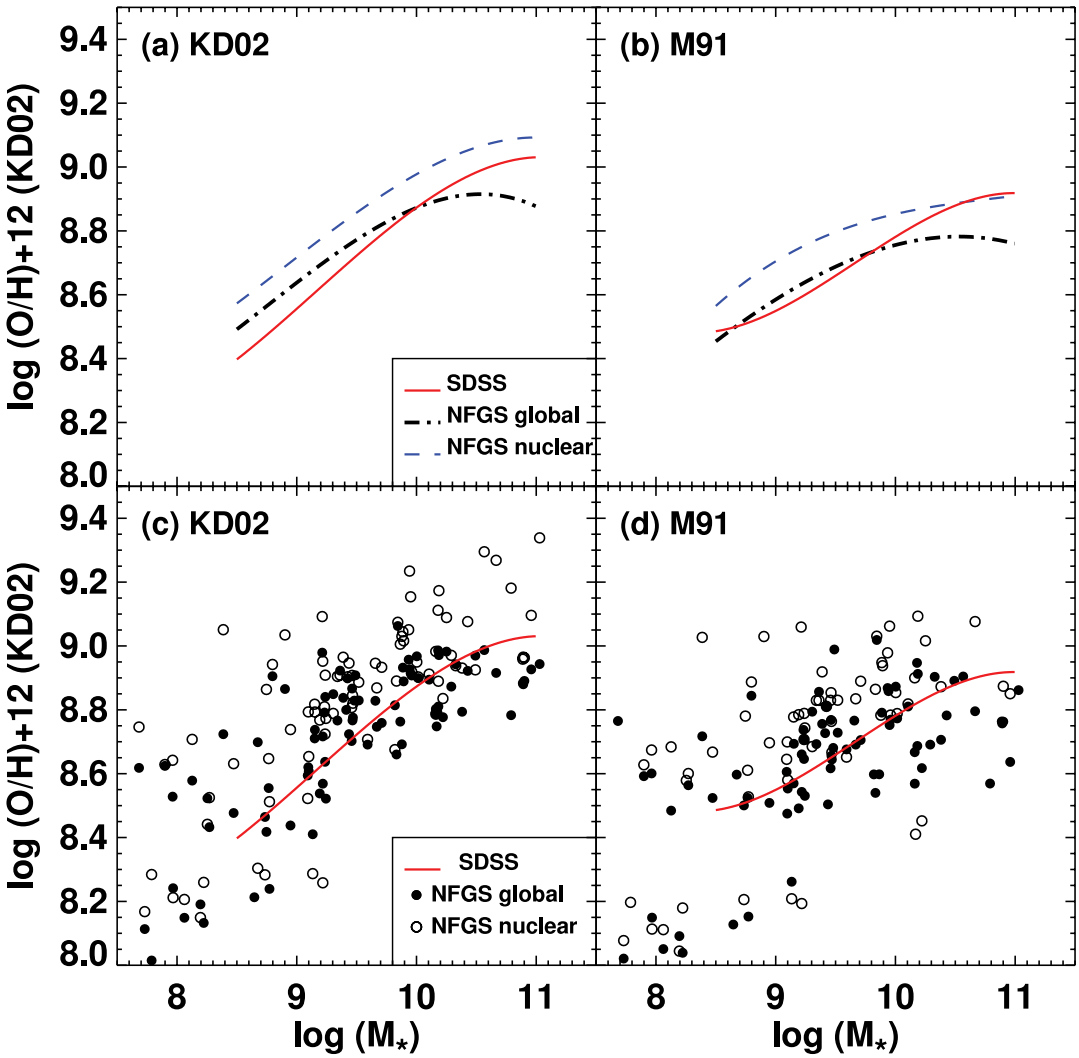


FIG. 7.—(*a*, *b*) Comparison between the robust best-fit SDSS *M-Z* relation (*red solid line*) and the best-fit relations to the NFGS nuclear (*blue dashed line*) and global (*black dot-dashed line*) relations. Metallicities were calculated using both (*a*) KD02 and (*b*) M91 calibrations, and stellar masses are given assuming a Salpeter IMF. (*c*, *d*) Comparison between the SDSS *M-Z* relation (*red solid line*) and the NFGS global (*filled circle*) and nuclear (*open circle*) data. At high stellar masses ($M_* > 10^{10}\ M_\odot$), the SDSS metallicities are ~0.1–0.15 dex larger than NFGS global metallicities at the same stellar mass.

results are obtained with the other strong-line methods. The SDSS *M-Z* relation lies in between the NFGS nuclear and global relations at high stellar masses ($M > 10^{10}\ M_\odot$). The NFGS global *M-Z* relation flattens at a metallicity that is ~0.1–0.15 dex smaller than the metallicity at which the SDSS relation flattens. This difference is not caused by metallicity calibration errors because the difference in upper turnoff is observed with all strong-line metallicity calibrations. Furthermore, the difference of $\log M = 0.17$ dex between the Bell & de Jong (2001) stellar mass relation and the SDSS Bruzual & Charlot (2003) model stellar masses cannot account for the difference between the SDSS and global NFGS *M-Z* relations.

The difference between the SDSS and NFGS *nuclear* and *M-Z* relations is probably driven by two factors: (1) fixed-size aperture differences and (2) different surface brightness profiles. The NFGS nuclear sample has a smaller mean covering fraction than the SDSS sample (~10% vs. ~34%), giving higher nuclear metallicities in the NFGS than for SDSS galaxies with the same stellar mass. In addition, the NFGS and SDSS samples have different surface brightness profiles (traced by their half-light radii). The NFGS sample has a slightly smaller mean half-light radius than our SDSS sample (~3.0 kpc vs. ~3.4 kpc). S. L. Ellison et al. (2008, in preparation) show that for the SDSS, galaxies with small $g'$-band half-light radii (i.e., more concentrated emission) have higher metallicities at a given mass than galaxies with large half-light radii (more diffuse emission).

The difference in half-light radii between the SDSS and NFGS samples cannot explain the difference between SDSS galaxies and *global* NFGS *M-Z* relations at high stellar masses $M_* > 10^{10}\ M_\odot$ because (1) the larger mean half-light radii of the SDSS sample would bias the SDSS toward lower metallicities than the NFGS (S. L. Ellison et al. 2008, in preparation) and (2) the NFGS global aperture covering fraction (~82%) captures most of the NFGS *B*-band emission. The half-light radius is irrelevant when the spectrum captures 100% of the *B*-band light.

We conclude that a $g'$-band covering fraction of ~20% (or lower redshift limit of $z = 0.04$) is insufficient for avoiding aperture bias in SDSS galaxies with stellar masses $M_* > 10^{10}\ M_\odot$. The mean covering fraction for $M_* > 10^{10}\ M_\odot$ galaxies is 30.6% ± 0.1%. A larger mean covering fraction is required to obtain a reliable *M-Z* relation at $M_* > 10^{10}\ M_\odot$.

## 9. DISCUSSION

We have investigated the effect of metallicity calibrations, AGN removal schemes, and a fixed-size aperture on the *M-Z*

TABLE 5

Relative Median Metallicity and rms Scatter for the Nine Strong-Line Metallicity Calibrations from 30,000 Random Sets of SDSS Galaxies

| ID | T04 (med/rms) | Z94 (med/rms) | KK04 (med/rms) | KD02 (med/rms) | M91 (med/rms) | D02 (med/rms) | PP04 (O3N2) (med/rms) | PP04 (N2) (med/rms) | P01 (med/rms) | Mean rms |
|---|---|---|---|---|---|---|---|---|---|---|
| T04 | ... | 0.006/0.08 | 0.053/0.09 | 0.033/0.07 | 0.036/0.09 | 0.076/0.10 | 0.040/0.08 | 0.053/0.09 | 0.046/0.14 | 0.09 |
| Z94 | −0.006/0.08 | ... | 0.046/0.05 | 0.023/0.05 | 0.024/0.04 | 0.062/0.09 | 0.029/0.06 | 0.042/0.08 | 0.034/0.11 | 0.07 |
| KK04 | −0.053/0.09 | −0.046/0.05 | ... | −0.023/0.05 | −0.014/0.02 | 0.016/0.06 | −0.017/0.05 | −0.003/0.07 | −0.004/0.09 | 0.06 |
| KD02 | −0.033/0.07 | −0.023/0.05 | 0.023/0.05 | ... | 0.005/0.05 | 0.039/0.06 | 0.006/0.05 | 0.019/0.05 | 0.011/0.10 | 0.06 |
| M91 | −0.036/0.09 | −0.024/0.04 | 0.014/0.02 | −0.005/0.05 | ... | 0.031/0.08 | −0.001/0.06 | 0.009/0.07 | 0.010/0.08 | 0.06 |
| D02 | −0.076/0.10 | −0.062/0.09 | −0.016/0.06 | −0.039/0.06 | −0.031/0.08 | ... | −0.033/0.05 | −0.020/0.03 | −0.017/0.11 | 0.07 |
| PP04 (O3N2) | −0.040/0.08 | −0.029/0.06 | 0.017/0.05 | −0.006/0.05 | 0.001/0.06 | 0.033/0.05 | ... | 0.014/0.05 | 0.012/0.12 | 0.07 |
| PP04 (N2) | −0.053/0.09 | −0.042/0.08 | 0.003/0.07 | −0.019/0.05 | −0.009/0.07 | 0.020/0.03 | −0.014/0.05 | ... | 0.004/0.11 | 0.07 |
| P01 | −0.046/0.14 | −0.034/0.11 | 0.004/0.09 | −0.011/0.10 | −0.010/0.08 | 0.017/0.11 | −0.012/0.12 | −0.004/0.11 | ... | 0.11 |

relation. The choice of metallicity calibration has the strongest effect on the *M-Z* relation. The choice of metallicity calibration changes the *y*-intercept of the *M-Z* relation significantly; the discrepancy between the metallicity calibrations is as large as 0.7 dex at the highest stellar masses. This discrepancy corresponds to a difference of 0.5–2.6 times solar at the peak metallicity of our SDSS sample.

The existence of a ~0.4–0.5 dex discrepancy between the $T_e$ and theoretical metallicities is well known (Stasińska 2002; Kennicutt et al. 2003; Garnett et al. 2004b). Our results show that the discrepancy is larger than previously thought. This discrepancy is often interpreted as an unknown problem with the photoionization codes used to calibrate the strong-line ratios with metallicity (Kennicutt et al. 2003; Garnett et al. 2004b; T04). However, recent investigations indicate that the $T_e$ methods may underestimate the metallicity when temperature fluctuations or gradients exist within the emission-line nebulae (Stasińska 2005; Bresolin 2006). These fluctuations, and hence the effect on $T_e$, are expected be the strongest at the highest metallicities. We conclude that for the metallicities spanned by the SDSS sample, it is not possible to know which (if any) metallicity calibration is correct. Until the metallicity discrepancies are resolved, only *relative* metallicity comparisons should be made.

Relative metallicity comparisons rely on the ability of strong-line calibrations to consistently reproduce the metallicity difference between any two galaxies. For example, if two galaxies have metallicities of $12 + \log(\mathrm{O/H}) = 8.4$ and $12 + \log(\mathrm{O/H}) = 8.9$ using one metallicity calibration, the difference in relative metallicities (0.5 dex) should be the same using any other metallicity calibration, even if the absolute metallicities differ from one calibration to another. We test how well the strong-line metallicity calibrations maintain relative metallicities by selecting 30,000 random sets of two galaxies from our SDSS sample. We measure the relative metallicity difference between the two galaxies from each set for each metallicity calibration. We give the mean difference in relative metallicity and rms residuals in Table 5. The mean difference in relative metallicity is $<0.07$ dex for all strong-line metallicity calibrations. The rms scatter is $\lesssim 0.15$ dex for all calibrations. The P05 method gives more discrepant relative metallicities to the other strong-line methods, with relative metallicity differences between 0.08 and 0.14 dex rms (cf. 0.02–0.11 dex rms). The best agreement between relative metallicities occurs between the three theoretical $R_{23}$ calibrations (M91; Z94; KK04), with relative metallicities agreeing to within 0.02–0.05 dex rms. The small difference and rms residuals in relative metallicities for all nine strong-line calibrations indicate that comparisons between galaxy or H II region metallicities can be reliably made to within ~0.15 dex, as long as the same base metallicity calibration is used for galaxies or H II regions. Our metallicity conversions aid relative metallicity comparisons between different samples of galaxies at different redshifts by empirically removing the discrepancy between each metallicity calibration. In practice, if relative metallicity differences between galaxies or between samples are $\lesssim 0.15$ dex, we recommend the use of two or more metallicity calibrations to verify that any difference observed is real, and not introduced by the metallicity calibration applied.

The SDSS sample is insufficient for determining the cause(s) of the metallicity discrepancy problem. Several ongoing investigations into the metallicity discrepancies may help solve this problem in the near future. These investigations include tailored photoionization models, high-S/N spectroscopy of luminous stars in the Milky Way and nearby galaxies, metal recombination lines, IR fine-structure lines, and temperature fluctuation studies.

Garnett et al. (2004a) applied tailored photoionization models to optical and infrared spectra of the H II region CCM 10 in M51. They found that the CCM 10 metallicity derived from the electron temperature using the infrared [O III] 88 $\mu$m line agrees with the theoretical metallicity computed with the latest version of the Cloudy version 90.4 photoionization code (Ferland et al. 1998). This theoretical metallicity is a factor of 2 smaller than the metallicity calculated with the previous version of Cloudy (ver. 74) that uses older atomic data. Clearly the optical emission line strengths in the photoionization models are very sensitive to the atomic data used. However, this sensitivity cannot explain the discrepancy observed in Figure 2 because T04 used the same version of Cloudy as Garnett et al. (2004a). In spite of the use of modern photoionization models with more accurate atomic data, the T04 *M-Z* relation lies significantly higher than the methods utilizing $T_e$ metallicities (P05; D02; PP04). Mathis & Wood (2005) used Monte Carlo photoionization models to show that different density distributions are not a significant source of error on the theoretical abundances. Recently, Ercolano et al. (2007) used new three-dimensional photoionization codes to investigate the effect of multiply noncentrally located stars on the temperature and ionization structure of H II regions. Ercolano et al. (2007) suggest that the geometrical distribution of ionizing sources may affect the metallicities derived using theoretical methods. Further theoretical investigations into the model assumptions, as well as tailored photoionization model fits to multiwavelength data of spatially resolved star-forming regions, may yield clues into whether the theoretical models contribute to the metallicity discrepancy.

High-S/N spectroscopy with 8–10 m telescopes can now provide metallicities for luminous stars and planetary nebulae in

nearby galaxies that can be compared with H II region metallicities (for a review see Przybilla et al. 2007). Urbaneja et al. (2005) analyzed the chemical composition of B-type supergiant stars in M33. They find that the supergiant metallicities agree with H II region abundances derived using the $T_e$ method. Similar results were obtained for local dwarf galaxies (Bresolin et al. 2006); however, other investigations require a correction for electron temperature fluctuations before agreement can be reached (Simón-Díaz et al. 2006).

Metal recombination lines provide a promising independent baseline for metallicity measurements because metal recombination lines depend only weakly on $T_e$ (see, e.g., Bresolin 2006). Metal recombination lines are weak, but they have been observed in H II regions in the Milky Way (Esteban et al. 2004, 2005; García-Rojas et al. 2005, 2006) and recently in nearby galaxies (Esteban et al. 2002; Peimbert et al. 2005). Recombination methods typically agree with theoretical methods (e.g., Bresolin 2006) and predict larger metallicities (by 0.2–0.3 dex) than the $T_e$ method. When the $T_e$ metallicities are corrected for electron temperature fluctuations, agreement is reached between recombination and $T_e$ methods (Peimbert et al. 2005, 2007; García-Rojas et al. 2005, 2006; López-Sánchez et al. 2007).

Measurements of electron temperature fluctuations in nearby H II regions can resolve the disagreement between strong-line theoretical methods and electron temperature methods (García-Rojas et al. 2006; Bresolin 2007) in most cases (see, however, Hägele et al. 2006). More electron temperature measurements are needed to verify these results, particularly for high-metallicity H II regions where electron temperature fluctuation measurements are lacking.

Despite these promising investigations, the metallicity discrepancy problem remains unsolved at the present time. Until the metallicity discrepancy problem is resolved, absolute metallicity values should be used with caution. In Table 5 we show that the metallicity calibrations maintain relative metallicities better than $\sim$0.15 dex rms, with the majority of theoretical methods maintaining relative metallicities within 0.04–0.1 dex rms. Therefore, studies of relative metallicity differences, such as comparisons between different galaxy samples, or between individual galaxies or H II regions, can be reliably made. If the size of the differences observed between different samples or different objects is $\sim$0.15 dex or less, we recommend the use of at least two independent calibrations to verify that the difference is calibration independent. The KD02 and PP04 methods give (1) low residual discrepancies in relative metallicities and (2) low residual discrepancy after other metallicities have been converted into these two methods. For the metallicity range of the SDSS sample, the KD02 and PP04 N2 calibrations are also independent of small contributions from an AGN. Because the KD02 and PP04 O3N2 methods maintain robust relative metallicities and are good base calibrations, we recommend the use of these two methods when deriving relative metallicities.

## 10. CONCLUSIONS

We present a detailed investigation into the *M-Z* relation for 27,730 star-forming galaxies from the SDSS. We apply 10 different metallicity calibrations to our SDSS sample, including theoretical photoionization calibrations and empirical $T_e$ method calibrations. We investigate the effect of these metallicity calibrations on the shape and *y*-intercept of the *M-Z* relation. Using 30,000 galaxy sets sampled randomly from our SDSS sample, we investigate how well the nine strong-line calibrations maintain relative metallicities. We find the following:

1. The choice of metallicity calibrations has the strongest effect on the *M-Z* relation. The choice of metallicity calibration can change the *y*-intercept of the *M-Z* relation by up to 0.7 dex. Until this metallicity discrepancy problem is resolved, absolute metallicities should be used with extreme caution.
2. There is considerable variation in shape and *y*-intercept of the *M-Z* relations derived using the empirical methods. We attribute this variation to the different H II region samples used to derive the empirical calibrations.
3. The relative difference in metallicities is maintained to an accuracy of $12 + \log(\mathrm{O/H}) \sim 0.02$–$0.1$ dex for 9/10 calibrations and to within $12 + \log(\mathrm{O/H}) \sim 0.15$ dex for all nine strong-line calibrations. For relative metallicity studies where the difference between targets or between samples is $\lesssim$0.15 dex, we recommend the use of at least two different calibrations to check that any result is not caused by the metallicity calibrations.

We use robust fits to the observed relationship between each metallicity calibration to derive new conversion relations for converting metallicities calculated using one calibration into metallicities of another, "base" calibration. We show that these conversion relations successfully remove the strong discrepancies observed in the *M-Z* relation between the different calibrations. Agreement is reached to within 0.03 dex on average.

We investigate the effect of AGN classification scheme and fixed-size aperture on the *M-Z* relation:

1. AGN classification methods have a negligible effect on metallicities derived using [N II]/[O II] or [N II]/H$\alpha$. AGN classification can affect metallicities derived with $R_{23}$ by $\lesssim$0.15 dex. For the SDSS sample, AGN classification methods make negligible difference in the shape or *y*-intercept of the *M-Z* relation. For samples containing a larger fraction of starburst-AGN composite galaxies, or samples where AGN removal is not possible, we recommend the use of [N II]/[O II] or [N II]/H$\alpha$ metallicity diagnostics.
2. The median $g'$-band aperture covering fraction of our SDSS sample is 34.2%. This covering fraction is insufficient for metallicities to represent global values at high masses ($M > 10^{10}\,M_{\odot}$). The NFGS global *M-Z* relation is 0.1–0.15 dex lower than the SDSS *M-Z* relation at $M > 10^{10}\,M_{\odot}$. Therefore, the metallicity at which the SDSS *M-Z* relation turns over is dependent on both the choice of metallicity calibration and the aperture size.

We recommend that metallicities be converted into either the PP04 method or the KD02 method to minimize any residual discrepancies and to maintain accurate relative metallicities compared to other calibrations. These two diagnostics have the added benefit that at high metallicities, the KD02 [N II]/[O II] and PP04 [N II]/H$\alpha$ calibrations are relatively independent of the method used to remove AGNs.

Future work into tailored photoionization models, high-S/N spectroscopy of luminous stars in the Milky Way and nearby galaxies, metal recombination lines, IR fine-structure lines, and temperature fluctuation studies may help resolve the metallicity discrepancy problem in the near future. Until then, only relative metallicity comparisons are reliable.

We thank Rolf Jansen for providing the $B - R$ colors for the NFGS. We thank Christy Tremonti for useful discussions. L. J. K. is supported by a Hubble Fellowship. S. L. E. acknowledges an NSERC Discovery grant that funded this research and is grateful to the IfA for hosting visits during which some of this work was completed. L. J. K. is grateful to the Aspen Center for Physics, where some of this work was done.

# APPENDIX A

## METALLICITY CALIBRATIONS: EQUATIONS AND METHOD

### A1. BREAKING THE $R_{23}$ DEGENERACY

Many empirical and theoretical metallicity calibrations rely on the ([O II] $\lambda$3727 + [O III] $\lambda\lambda$4959, 5007)/H$\beta$ line ratio, known as $R_{23}$. The major drawback to using $R_{23}$ is that it is double valued with metallicity; $R_{23}$ gives both a low metallicity estimate ("lower branch") and a high estimate ("upper branch") for most values of $R_{23}$ (for a discussion see, e.g., KK04). Additional line ratios, such as [N II]/H$\alpha$ or [N II]/[O II], are required to break this degeneracy.

The SDSS catalog contains very few metal-poor galaxies (Izotov et al. 2004, 2006a; Kniazev et al. 2003, 2004; Papaderos et al. 2006). Metal-poor galaxies are often lacking in magnitude-limited emission-line surveys because they are intrinsically rare, compact, and faint (e.g., Terlevich et al. 1991; Masegosa et al. 1994; van Zee 2000). For the purpose of investigating the upper and lower $R_{23}$ branches, we supplement the SDSS sample with (1) the low-metallicity galaxy sample described in Kewley et al. (2007) and Brown et al. (2006) and (2) the Kong & Cheng (2002) blue compact galaxy sample.

Note that we do not calculate an initial metallicity from an [N II]/H$\alpha$ or [N II]/[O II] metallicity calibration because in some cases, a systematic discrepancy between a metallicity calibration based on [N II]/H$\alpha$ or [N II]/[O II] and the calibration based on $R_{23}$ will cause galaxies to be improperly placed on the upper or lower branch of $R_{23}$. For example, an [N II]/H$\alpha$ metallicity calibration that systematically produces higher estimates than the subsequent $R_{23}$ calibration may cause metallicities to be erroneously estimated from the upper $R_{23}$ branch.

We use the [N II]/[O II] ratio to break the $R_{23}$ degeneracy for our SDSS sample. The [N II]/[O II] ratio is not sensitive to the ionization parameter to within $\pm$0.05 dex, and it is a strong function of metallicity above $\log([\mathrm{N\ II}]/[\mathrm{O\ II}]) \gtrsim -1.2$ (KD02). The top panel of Figure 8 shows that the division between the $R_{23}$ upper and lower branches occurs at $\log([\mathrm{N\ II}]/[\mathrm{O\ II}]) \sim -1.2$ for the SDSS and supplementary samples. For comparison, the bottom panel of Figure 8 shows the theoretical relationship between [N II]/[O II] and $R_{23}$ using the population synthesis and photoionization models of KD02. The observed $R_{23}$ peak at $\log([\mathrm{N\ II}]/[\mathrm{O\ II}]) \sim -1.2$ corresponds to a metallicity of $12 + \log(\mathrm{O/H}) \sim 8.4$ according to the theoretical models.

For galaxies at high redshift, the [N II]/[O II] ratio cannot be used to break the $R_{23}$ degeneracy because either (1) [N II]/[O II] cannot be corrected for extinction due to a lack of reliable Balmer line ratios and/or (2) [N II] and [O II] are not observed simultaneously in a given spectrum. In this case the [N II]/H$\alpha$ ratio is used (Fig. 9). The top panel of Figure 9 shows that the division between the $R_{23}$ upper and lower branches occurs between $-1.3 < \log([\mathrm{N\ II}]/\mathrm{H}\alpha) \lesssim -1.1$ for the SDSS and supplementary samples. The division between the upper and lower $R_{23}$ branches using [N II]/H$\alpha$ (Fig. 9, *top panel*) is less clear than for [N II]/[O II] (Fig. 8, *top panel*) because the [N II]/H$\alpha$ ratio is less sensitive to metallicity, and more sensitive to ionization parameter, than [N II]/[O II].

We check whether our empirical [N II]/H$\alpha$ division between the upper and lower $R_{23}$ branches [$-1.3 < \log([\mathrm{N\ II}]/\mathrm{H}\alpha) \lesssim -1.1$] is compatible with our [N II]/[O II] division [$\log([\mathrm{N\ II}]/[\mathrm{O\ II}]) \lesssim -1.2$] by comparing the number of galaxies placed on the upper

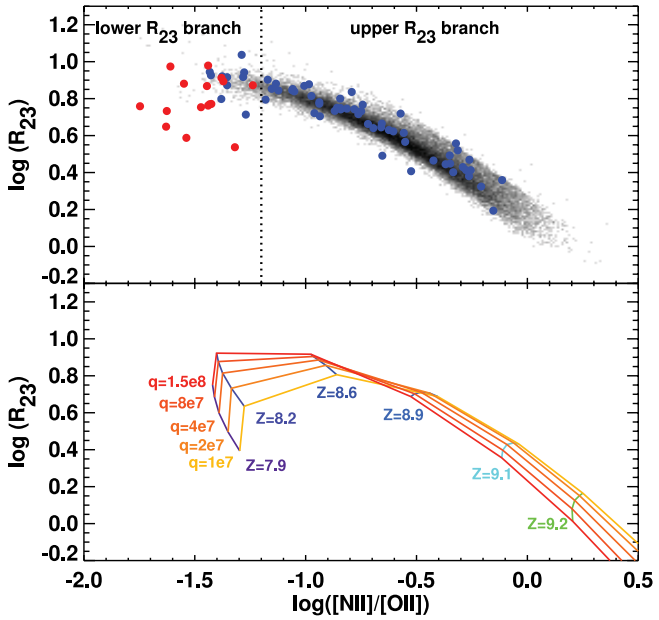


Fig. 8.—*Top*: Observed relationship between the metallicity-sensitive [N II] $\lambda$6584/[O II] $\lambda$3727 line ratio and the commonly used ([O II] $\lambda$3727 + [O III] $\lambda\lambda$4959, 5007)/H$\beta$ ratio. The SDSS galaxies (*black*), the Kong & Cheng (2002) blue compact galaxy sample (*blue*), and the Brown et al. (2006) low-metallicity galaxy sample (*red*) are shown. The [N II]/[O II] ratio is a strong monotonic function of metallicity to $\log([\mathrm{N\ II}]/[\mathrm{O\ II}]) \gtrsim -1.2$, while $R_{23}$ has a maximum at $\log R_{23} \sim 0.9$. For our samples, the $R_{23}$ maximum is likely to occur at $\log([\mathrm{N\ II}]/[\mathrm{O\ II}]) \sim -1.2$. This value can be used to break the $R_{23}$ degeneracy for galaxies where [N II]/[O II] can be corrected for extinction using the Balmer decrement. *Bottom*: Theoretical relationship between the [N II]/[O II] and $R_{23}$ line ratios using the stellar population synthesis and photoionization model grids of KD02. Models are shown for constant metallicities of $12 + \log(\mathrm{O/H}) = 7.9$, 8.2, 8.6, 8.9, 9.1, and 9.2 and ionization parameters of $q = 1 \times 10^7$, $2 \times 10^7$, $4 \times 10^7$, $8 \times 10^7$, and $1.5 \times 10^8$ cm s$^{-1}$. We choose a break between the $R_{23}$ upper and lower branches at $\log([\mathrm{N\ II}]/[\mathrm{O\ II}]) \sim -1.2$, which corresponds to a metallicity of $12 + \log(\mathrm{O/H}) \sim 8.4$ according to the theoretical models.

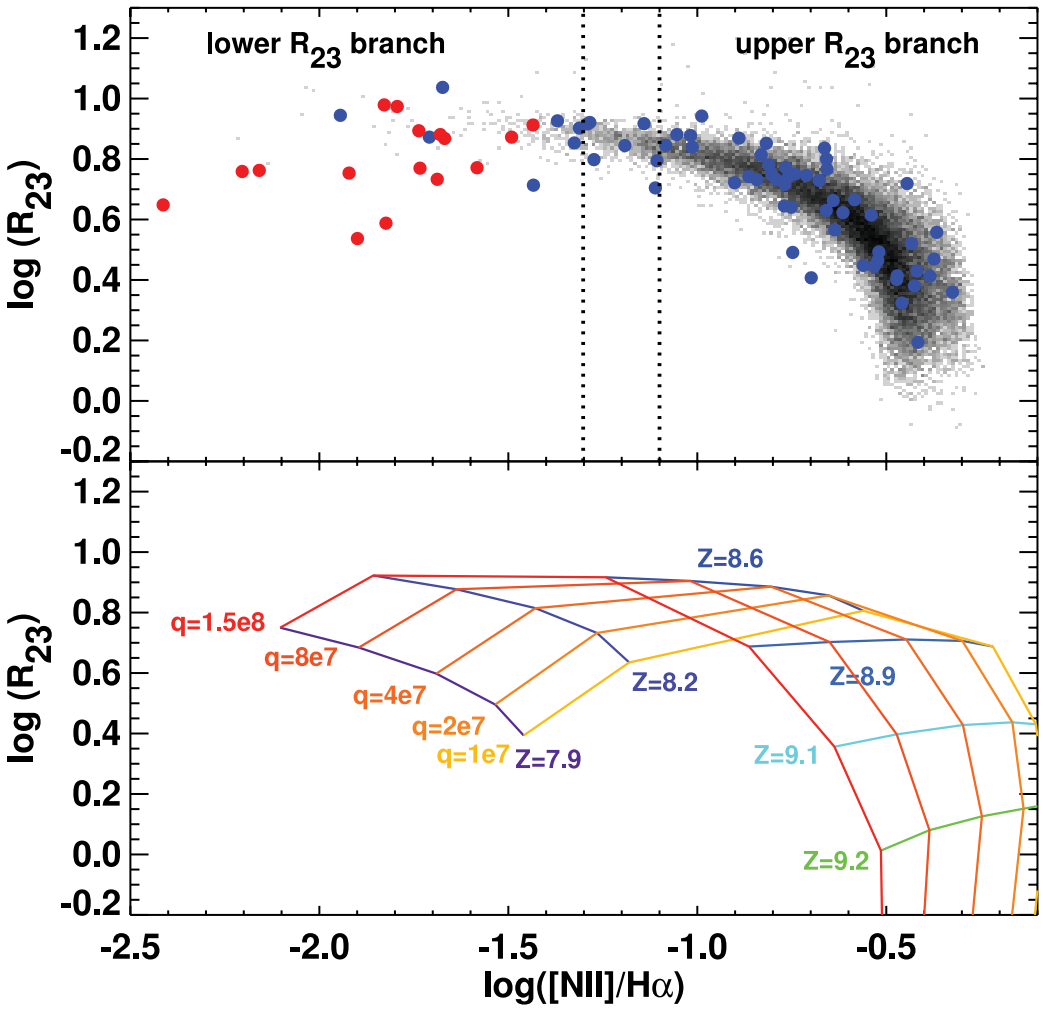


FIG. 9.—*Top*: Observed relationship between the metallicity-sensitive [N II] $\lambda$6584/H$\alpha$ line ratio and the commonly used ([O II] $\lambda$3727 + [O III] $\lambda\lambda$4959, 5007)/H$\beta$ ratio. The SDSS galaxies (*black*), the Kong & Cheng (2002) blue compact galaxy sample (*blue*), and the Brown et al. (2006) low-metallicity galaxy sample (*red*) are shown. For $\log([\mathrm{N\ II}]/\mathrm{H}\alpha) \gtrsim -1.1$, galaxies are likely to lie on the upper $R_{23}$ branch. For $-1.3 < \log([\mathrm{N\ II}]/\mathrm{H}\alpha) < -1.1$, [N II]/H$\alpha$ cannot discriminate between the upper and lower $R_{23}$ branches. For $\log([\mathrm{N\ II}]/\mathrm{H}\alpha) \lesssim -1.3$, galaxies lie on the lower $R_{23}$ branch. *Bottom*: Theoretical relationship between the [N II]/[O II] and $R_{23}$ line ratios using the stellar population synthesis and photoionization model grids of KD02. Models are shown for constant metallicities of $12 + \log(\mathrm{O/H}) = 7.9$, 8.2, 8.6, 8.9, 9.1, and 9.2 and ionization parameters of $q = 1 \times 10^7$, $2 \times 10^7$, $4 \times 10^7$, $8 \times 10^7$, and $1.5 \times 10^8$ cm s$^{-1}$.

and lower branches using each ratio. For $\log([\mathrm{N\ II}]/\mathrm{H}\alpha) \lesssim -1.3$, the majority of galaxies (150/175; 86%) lie on the lower $R_{23}$ branch according to their [N II]/[O II] line ratios. For $\log([\mathrm{N\ II}]/\mathrm{H}\alpha) \gtrsim -1.1$, the upper $R_{23}$ branch can be clearly seen. For $-1.3 < \log([\mathrm{N\ II}]/\mathrm{H}\alpha) < -1.1$, [N II]/H$\alpha$ cannot discriminate between the upper and lower $R_{23}$ branches. The bottom panel of Figure 9 shows that galaxies with $-1.3 < \log([\mathrm{N\ II}]/\mathrm{H}\alpha) < -1.1$ are likely to have metallicities that are close to the $R_{23}$ maximum. For the SDSS galaxies with $-1.3 < \log([\mathrm{N\ II}]/\mathrm{H}\alpha) < -1.1$ in the top panel of Figure 9, the [N II]/[O II] ratios indicate that 634/1127 (56%) of SDSS galaxies lie on the upper branch and 493/1127 (44%) of SDSS galaxies lie on the lower branch.

For the $R_{23}$ methods in this paper, we use the [N II]/[O II] line ratio to break the $R_{23}$ degeneracy.

## A2. THEORETICAL PHOTOIONIZATION METHODS

### A2.1. M91

The M91 calibration of $R_{23}$ is based on detailed H II region models using the photoionization code Cloudy (Ferland et al. 1998). The M91 calibration includes a correction for ionization parameter variations. We use the [N II]/[O II] line ratio to break the $R_{23}$ degeneracy, as described in § A1, and we apply the analytic expressions for the M91 lower and upper branches given in Kobulnicky et al. (1999):

$$12 + \log(\mathrm{O/H})_{\mathrm{lower}} = 12 - 4.944 + 0.767x + 0.602x^2 - y(0.29 + 0.332x - 0.331x^2), \quad \text{(A1)}$$

$$12 + \log(\mathrm{O/H})_{\mathrm{upper}} = 12 - 2.939 - 0.2x - 0.237x^2 - 0.305x^3 - 0.0283x^4 - y(0.0047 - 0.0221x - 0.102x^2 - 0.0817x^3 - 0.00717x^4), \quad \text{(A2)}$$

where $x = \log R_{23} = \log [([\mathrm{O\ II}]\ \lambda3727 + [\mathrm{O\ III}]\ \lambda4959 + [\mathrm{O\ III}]\ \lambda5007)/\mathrm{H}\beta]$ and $y = \log O_{32} = \log [([\mathrm{O\ III}]\ \lambda4959 + [\mathrm{O\ III}]\ \lambda5007)/[\mathrm{O\ II}]\ \lambda3727]$. The estimated accuracy of the M91 calibration is $\sim$0.15 dex.

### A2.2. KD02

The KD02 calibrations are based on a self-consistent combination of detailed stellar population synthesis and photoionization models. The estimated accuracy of the KD02 calibrations is $\sim$0.1 dex. This estimate is derived by varying the major assumptions in the stellar evolution and photoionization models (including the star formation prescription, electron density, and the IMF). KD02 outlined a "recommended" approach to deriving metallicities that uses the [N II]/[O II] line ratio for high metallicities and a combination of $R_{23}$ calibrations for lower metallicities. We use a revised version of the KD02 calibration. For $\log([\mathrm{N\ II}]/[\mathrm{O\ II}]) > -1.2$, we use the original KD02 [N II]/[O II] metallicity calibration given by

$$\log([\mathrm{N\ II}]/[\mathrm{O\ II}]) = 1106.8660 - 532.15451Z + 96.373260Z^2 - 7.8106123Z^3 + 0.23928247Z^4, \quad \text{(A3)}$$

where $Z = \log(\mathrm{O/H}) + 12$. We use the IDL task `fz_roots` to solve the fourth-order polynomial for $Z$. The coefficients in equation (A3) are based on the theoretical $q = 2 \times 10^7$ cm s$^{-1}$ relationship between [N II]/[O II] and $Z$. However, the detailed relationship between [N II]/[O II] and $Z$ is independent of ionization parameter to within $\sim$0.1 dex for $\log([\mathrm{N\ II}]/[\mathrm{O\ II}]) > -1.2$ and the ionization parameters covered by the SDSS ($q = 1 \times 10^7$–$8 \times 10^7$ cm s$^{-1}$).

For $\log([\mathrm{N\ II}]/[\mathrm{O\ II}]) < -1.2$ [or $12 + \log(\mathrm{O/H}) < 8.4$; KD02], KD02 recommend using an average of $R_{23}$ methods. In this regime, we use the average of the KK04 lower branch $R_{23}$ calibration (eq. [A6]) and the lower branch M91 $R_{23}$ calibration (eq. [A1]). Both of these calibrations correct for ionization parameter variations.

### A2.3. KK04

KK04 use the stellar evolution and photoionization grids from KD02 to produce an improved fit to the $R_{23}$ calibration. The estimated accuracy of the KK04 method is $\sim$0.15 dex.

The $R_{23}$ calibration is sensitive to the ionization state of the gas, particularly for low metallicities where the $R_{23}$ line ratio is not a strong function of metallicity. The ionization state of the gas is characterized by the ionization parameter, defined as the number of hydrogen-ionizing photons passing through a unit area per second, divided by the hydrogen density of the gas. The ionization parameter $q$ has units of cm s$^{-1}$ and can be thought of as the maximum velocity ionization front that a radiation field is able to drive through the nebula. The ionization parameter is typically derived using the [O III]/[O II] line ratio. This ratio is sensitive to metallicity and therefore KK04 recommend an iterative approach to derive a consistent ionization parameter and metallicity solution. We first use the [N II]/[O II] ratio to determine whether each SDSS galaxy lies on the upper or lower $R_{23}$ branch. We then calculate an initial ionization parameter by assuming a nominal lower branch [$12 + \log(\mathrm{O/H}) = 8.2$] or upper branch [$12 + \log(\mathrm{O/H}) = 8.7$] metallicity using equation (13) from KK04, i.e.,

$$\log q = \left\{32.81 - 1.153y^2 + [12 + \log(\mathrm{O/H})]\left(-3.396 - 0.025y + 0.1444y^2\right)\right\} \times \left\{4.603 - 0.3119y - 0.163y^2 + [12 + \log(\mathrm{O/H})]\left(-0.48 + 0.0271y + 0.02037y^2\right)\right\}^{-1}, \quad \text{(A4)}$$

where $y = \log O_{32} = \log([\mathrm{O\ III}]\ \lambda5007/[\mathrm{O\ II}]\ \lambda3727)$. The initial resulting ionization parameter is used to derive an initial metallicity estimate from equation (16) of KK04 for $\log([\mathrm{N\ II}]/[\mathrm{O\ II}]) < -1.2$ [$12 + \log(\mathrm{O/H}) \lesssim 8.4$], or equation (17) of KK04 for $\log([\mathrm{N\ II}]/[\mathrm{O\ II}]) > -1.2$ [$12 + \log(\mathrm{O/H}) \gtrsim 8.4$]:

$$12 + \log(\mathrm{O/H})_{\mathrm{lower}} = 9.40 + 4.65x - 3.17x^2 - \log q\left(0.272 + 0.547x - 0.513x^2\right), \quad \text{(A5)}$$

$$12 + \log(\mathrm{O/H})_{\mathrm{upper}} = 9.72 - 0.777x - 0.951x^2 - 0.072x^3 - 0.811x^4x - \log q\left(0.0737 - 0.0713x - 0.141x^2 + 0.0373x^3 - 0.058x^4\right), \quad \text{(A6)}$$

where $x = \log R_{23} = \log [([\mathrm{O\ II}]\ \lambda3727 + [\mathrm{O\ III}]\ \lambda\lambda4959,\ 5007)/\mathrm{H}\beta]$. Equations (A4) and (A6) (or eq. [A5]) are iterated until $12 + \log(\mathrm{O/H})$ converges. Three iterations are typically required to reach convergence.

### A2.4. Z94

The Z94 calibration is based on the $R_{23}$ line ratio. This calibration is derived from the average of three previous calibrations by Edmunds & Pagel (1984), Dopita & Evans (1986), and McCall et al. (1985). The uncertainty in the Z94 calibration is estimated by the difference in metallicity estimates between the three calibrations. Z94 provide a polynomial fit to their calibration that is only valid for the upper $R_{23}$ branch [i.e., $12 + \log(\mathrm{O/H}) > 8.4$, or $\log([\mathrm{N\ II}]/[\mathrm{O\ II}]) > -1.2$]:

$$12 + \log(\mathrm{O/H}) = 9.265 - 0.33x - 0.202x^2 - 0.207x^3 - 0.333x^4, \quad \text{(A7)}$$

where $x = \log R_{23} = \log [([\mathrm{O\ II}]\ \lambda3727 + [\mathrm{O\ III}]\ \lambda\lambda4959,\ 5007)/\mathrm{H}\beta]$. A solution for the ionization parameter is not explicitly included in the Z94 calibration.

### A2.5. T04

T04 estimated the metallicity for each galaxy statistically based on theoretical model fits to the strong emission lines [O II], H$\beta$, [O III], H$\alpha$, [N II], and [S II]. The model fits were calculated using a combination of stellar population synthesis models from Bruzual & Charlot (2003) and Cloudy photoionization models from Ferland et al. (1998). The T04 scheme is more sophisticated than the other theoretical methods because it takes advantage of all of the strong emission lines in the optical spectrum, allowing more constraints to be made on the model parameters. Calibrations of various line ratios to the theoretical T04 method are given by Nagao et al. (2006) and Liang et al. (2006). We use the original T04 metallicities, available online.[4]

## A3. $T_e$ METHOD

We derive the gas-phase oxygen abundance following the procedure outlined in Izotov et al. (2006b). This procedure utilizes the electron temperature ($T_e$) calibrations of Aller (1984) and the atomic data compiled by Stasińska (2005). Abundances are determined within the framework of the classical two-zone H II region model (Stasińska 1980). The ratio of the auroral [O III] $\lambda$4363 and [O III] $\lambda\lambda$4959, 5007 emission lines gives an electron temperature in the $O^{++}$ zone. We derive electron densities measured using the [S II] $\lambda$6717/[S II] $\lambda$6731 line ratio. These electron temperatures are insensitive to small variations in electron density; we obtain the same $T_e$ with an electron density of 367 cm$^{-3}$. The electron temperature of the $O^+$ zone is calculated assuming $T_e(O^+) = 0.7T_e(O^{++}) + 0.3$ (Stasińska 1980). We calculate the metallicity in the $O^+$ and $O^{++}$ zones assuming

$$\mathrm{O/H} = \mathrm{O^+/H^+} + \mathrm{O^{++}/H^+}. \tag{A8}$$

The uncertainty in the absolute O/H metallicity determination by this $T_e$ method is $\sim$0.1 dex. This intrinsic uncertainty is the dominant error in our $T_e$ metallicity determination and includes errors in the use of simplified H II region models and possible problems with electron temperature fluctuations (Pagel & Tautvaisiene 1997). Fortunately, these errors affect all $T_e$-based methods in a similar way and the error in relative metallicities derived using the same method is likely to be $\ll$0.1 dex.

This "classical" $T_e$ approach does not take unseen stages of ionization or electron temperature fluctuations into account. Bresolin (2006) notes that if electron temperature fluctuations are substantial and are not taken into account, $T_e$-based calibrations can only provide a lower limit to the true metallicity, particularly in the high-metallicity regime where $T_e$ fluctuations appear stronger. We find that the $T_e$ method does not produce any SDSS metallicities of solar [12 + log (O/H) $\sim$ 8.69; Allende Prieto et al. 2001; Asplund et al. 2004] or above, even for galaxies where the fiber only captures 20%–30% of the central $g'$-band galaxy light. Covering fractions of 20%–30% correspond to diameters of $\sim$5 kpc for the mean size of nearby star-forming galaxies (Kewley et al. 2005). Spiral galaxies typically have metallicities within similar apertures that are $\sim$1–2 times solar, measured using various independent methods (for a review see Henry & Worthey 1999). For example, our Galaxy has consistent central metallicities within the central $\sim$5 kpc of 1–2 times solar from studies of planetary nebulae (Martins & Viegas 2000), IR fine-structure lines in H II regions (Simpson et al. 1995; Afflerbach et al. 1997), and radio recombination lines (Quireza et al. 2006).

We conclude that $T_e$ metallicities should be used with caution when other line ratios (such as [N II]/H$\alpha$ and [N II]/[O II]) indicate upper branch (Figs. 8 and 9) or supersolar metallicities.

## A4. EMPIRICAL $T_e$ FIT METHODS

H II regions with $T_e$-based metallicities have been used in many studies to derive empirical fits to strong-line ratios that can be applied to H II regions and galaxies where the [O III] $\lambda$4363 line is not observed.

### A4.1. PP04 O3N2 and N2

PP04 derived two new methods for measuring metallicities in galaxies at high redshift. At high redshift, obtaining a reddening estimate is difficult and in some cases impossible, and flux calibration in the infrared is nontrivial. Ratios of lines that are very close in wavelength do not require reddening correction or flux calibration. PP04 fit the observed relationships between [N II]/H$\alpha$, ([O II]/H$\beta$)/([N II]/H$\alpha$), and the $T_e$-based metallicity for a sample of 137 H II regions. Of these 137 H II regions, 131 have $T_e$-based metallicities and 6 high-metallicity H II regions have metallicities derived using detailed photoionization models. Because the vast majority of H II regions in the PP04 sample have $T_e$-based metallicities, we refer to the PP04 method as an empirical $T_e$ fit method. The fit to the relationship between $T_e$ metallicities and the ([O II]/H$\beta$)/([N II]/H$\alpha$) ratio is

$$12 + \log(\mathrm{O/H}) = 8.73 - 0.32 \times \mathrm{O3N2}, \tag{A9}$$

where O3N2 is defined as O3N2 = log [([O III] $\lambda$5007/H$\beta$)/([N II] $\lambda$6584/H$\alpha$)]. Equation (A9) is only valid for O3N2 $< 2$. We refer to this calibration as "PP04 O3N2."

PP04 fitted the relationship between $T_e$ metallicities and the [N II]/H$\alpha$ ratio by a line and a third-order polynomial. We use the polynomial fit given by

$$12 + \log(\mathrm{O/H}) = 9.37 + 2.03 \times \mathrm{N2} + 1.26 \times \mathrm{N2}^2 + 0.32 \times \mathrm{N2}^3, \tag{A10}$$

where N2 is defined as N2 = log ([N II] $\lambda$6584/H$\alpha$). Equation (A10) is valid for $-2.5 <$ N2 $< -0.3$.

[4] See http://www.mpa-garching.mpg.de/SDSS/.

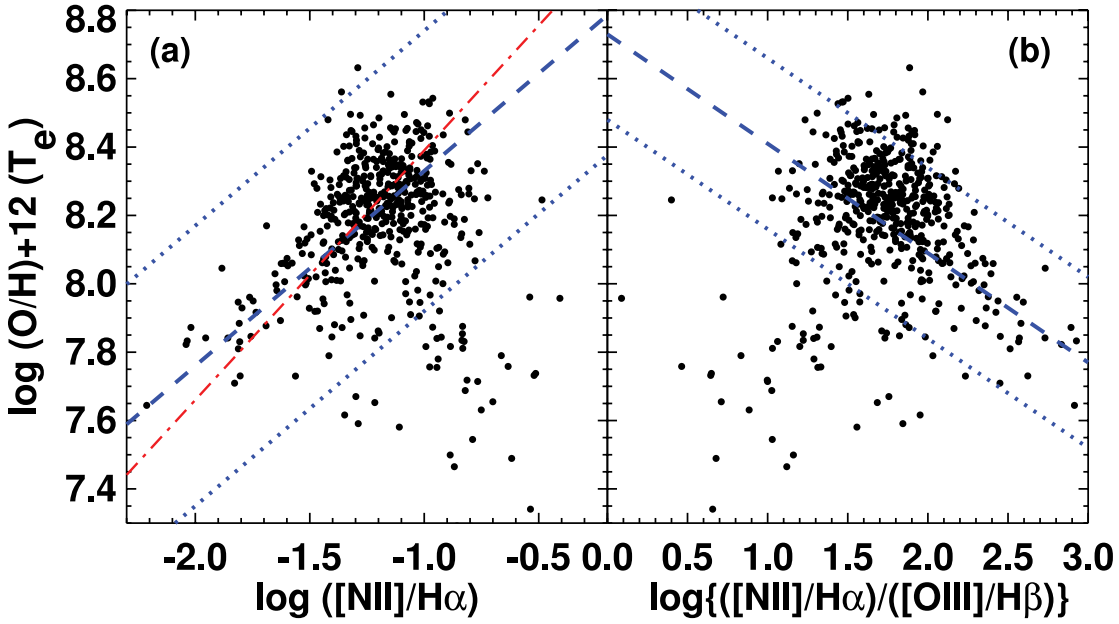


FIG. 10.—Observed relationship between the metallicities derived using the $T_e$ method and (*a*) the [N II] $\lambda$6584/H$\alpha$ line ratio and (*b*) the ([O II]/H$\beta$)/([N II]/H$\alpha$) ratio. SDSS galaxies with usable [O III] $\lambda$4363 line fluxes (S/N $>$ 3) are shown as black filled circles. The PP04 calibration (*dashed lines*) and 95th percentile lines (*dotted lines*) are shown for each line ratio. The D02 calibration (*red dot-dashed line*) is shown for panel (*a*). A fraction of SDSS $T_e$ galaxies have $T_e$ metallicities that lie below the 95th percentile line in both the [N II]/H$\alpha$ and ([O II]/H$\beta$)/([N II]/H$\alpha$) diagrams. These galaxies have high [N II]/H$\alpha$ and [N II]/[O II] ratios, suggesting high (above solar) metallicities. The $T_e$ method appears to underestimate the metallicity in these galaxies, possibly as a result of temperature gradients or fluctuations that may occur preferentially at high metallicities.

Because the PP04 method was derived using a fit to H II regions rather than galaxies, we check whether the PP04 relations are suitable for metallicity estimates of the SDSS sample. In Figure 10 we show the relationship between (1) N2 and $T_e$ metallicities and (2) O3N2 and $T_e$ metallicities for the SDSS galaxies in our sample with measurable (S/N $>$ 3) [O III] $\lambda$4363 lines. The dashed line indicates the PP04 calibrations based on H II regions, while the dotted lines encompass 95% of the H II regions in the PP04 sample. The majority of the SDSS galaxies lie within the PP04 95th percentile lines. However, 47/546 (9%) and 69/546 (13%) of SDSS $T_e$ galaxies have $T_e$ metallicities that lie below the 95th percentile line in the N2 and N2O3 diagrams, respectively. These galaxies have high [N II]/H$\alpha$ and [N II]/[O II] ratios [log ([N II]/H$\alpha$) $> -1$; log ([N II]/[O II]) $> -0.8$], indicating supersolar metallicities, according to all of the [N II]/H$\alpha$– and [N II]/[O II]–based metallicity diagnostics. Both Figure 10 and the high [N II]/H$\alpha$ and [N II]/[O II] ratios suggest that the $T_e$ method underestimates metallicities for galaxies that lie below the PP04 95th percentile line.

### A4.2. P05

P01 derived an empirical calibration for $R_{23}$ based on $T_e$ metallicities for a sample of H II regions. This calibration has been updated by P05 using a larger sample of H II regions. They perform fits to the relationship between $R_{23}$ and $T_e$ metallicities that includes an excitation parameter $P$ that corrects for the effect of ionization parameter. The resulting calibration has an upper branch calibration that is valid for $T_e$-based metallicities $12 + \log(\mathrm{O/H}) > 8.25$ and a lower branch calibration that is valid for $T_e$-based metallicities $12 + \log(\mathrm{O/H}) < 8.0$. We use the [N II]/[O II] ratio (Fig. 8) to discriminate between the upper and lower branches for P05, and we apply the appropriate upper and lower branch calibrations (eqs. [22] and [24] of P05):

$$12 + \log(\mathrm{O/H})_{\mathrm{upper}} = \frac{R_{23} + 726.1 + 842.2P + 337.5P^2}{85.96 + 82.76P + 43.98P^2 + 1.793R_{23}}, \tag{A11}$$

$$12 + \log(\mathrm{O/H})_{\mathrm{lower}} = \frac{R_{23} + 106.4 + 106.8P - 3.40P^2}{17.72 + 6.60P + 6.95P^2 - 0.302R_{23}}, \tag{A12}$$

where $R_{23} = ([\mathrm{O\ II}]\ \lambda\lambda 3727,\ 3729 + [\mathrm{O\ III}]\ \lambda\lambda 4959,\ 5007)/\mathrm{H}\beta$ and $P = ([\mathrm{O\ III}]\ \lambda\lambda 4959,\ 5007/\mathrm{H}\beta)/R_{23}$. P05 estimate that the accuracy for reproducing $T_e$-based metallicities with the P05 calibration is $\sim$0.1 dex.

Because the P05 method was derived using fits to H II regions, we test whether the P05 method is applicable to the relationship between the SDSS $T_e$ metallicities and $R_{23}$ in Figure 11. In Figure 11*a* we plot all SDSS galaxies in our sample with S/N $>$ 3 in the [O III] $\lambda$4363 line. The upper and lower P05 branches are shown for different values of the excitation parameter $P$ (*red dot-dashed lines*). Several galaxies lie outside the bounds of the P05 lower branch [$12 + \log(\mathrm{O/H})(T_e) < 8.0$].

In Figure 11*b* we exclude the galaxies that lie below the lowest 95th percentile line in the PP04 O3N2 calibration (Fig. 10*b*), which are likely to have unreliable $T_e$ metallicities. As we discussed in § A4.1, these excluded galaxies with [N II]/H$\alpha$ and [N II]/[O II] ratios that indicate metallicities above solar. We note that the excluded galaxies have excitation parameters between $0.2 < P < 0.8$, with a mean excitation parameter of $0.46 \pm 0.03$. These $P$-values are more consistent with the P05 upper branch (range $0.2 < P < 0.8$, mean $0.64 \pm 0.03$) than the P05 lower branch (range $0.6 < P < 1.0$, mean $0.8 \pm 0.1$) for our SDSS sample. The $T_e$ method may not be reliable for these galaxies.

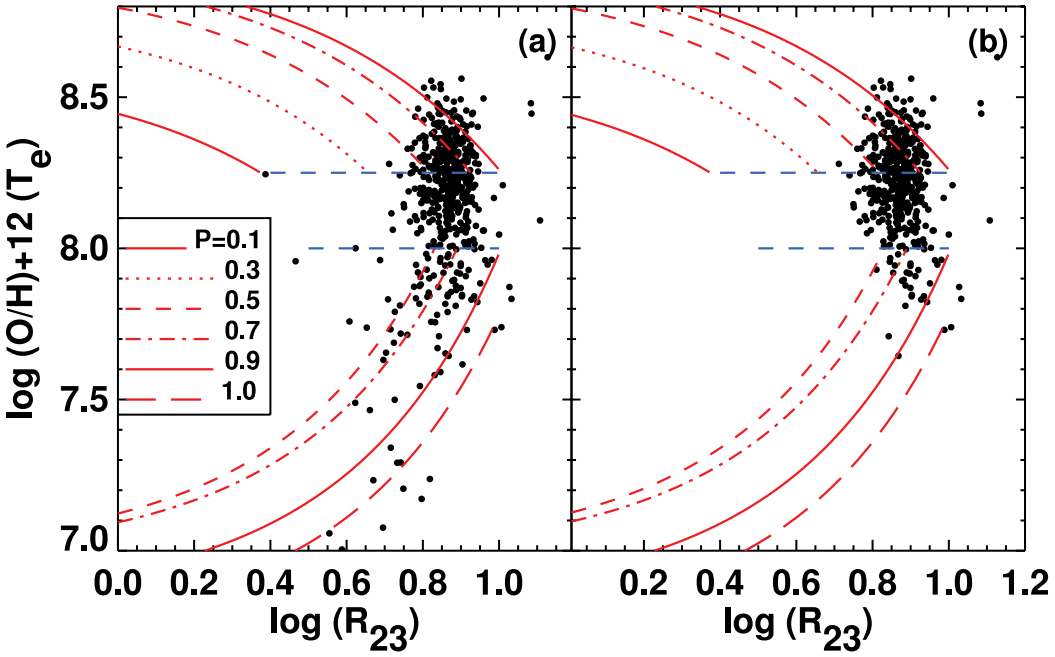


FIG. 11.—Observed relationship between the metallicities derived using the $T_e$ method and the $R_{23}$ line ratio for (*a*) all SDSS galaxies in our sample with measurable (S/N > 3) [O III] $\lambda$4363 fluxes and (*b*) the SDSS galaxies in our sample with measurable [O III] $\lambda$4363 lines that lie above the lowest 95th percentile line in the PP04 O3N2 calibration (Fig. 10).

## A5. COMBINED $T_e$–STRONG-LINE METHOD

### A5.1. D02

The D02 calibration is based on a fit to the relationship between the $T_e$ metallicities and the [N II]/H$\alpha$ line ratio for ~155 H II regions. Of these H II regions, ~100 have metallicities derived using the $T_e$ method and 55 have metallicities estimated using the theoretical M91 $R_{23}$ method, or an empirical method proposed by Díaz & Pérez-Montero (2000) based on the sulfur lines. The division between H II regions with $T_e$-based metallicities and those with strong-line metallicities occurs at $12 + \log(\mathrm{O/H}) \sim 8.4$. The D02 calibration is given by a linear least-squares fit:

$$12 + \log(\mathrm{O/H}) = 9.12 + 0.73 \times \mathrm{N2}, \tag{A13}$$

where N2 = log ([N II] $\lambda$6584/H$\alpha$). D02 estimate that the uncertainty in the derived metallicities is ~0.2 dex.

In Figure 10 we compare the D02 fit (*red dot-dashed line*) to the [N II]/H$\alpha$–$T_e$ relationship for the SDSS galaxies. The D02 method provides a reasonable fit to the SDSS galaxies, given the large scatter, and is similar to the PP04 N2 curve to within ~0.2 dex over the metallicity range $7.4 < 12 + \log(\mathrm{O/H}) < 8.8$.

## APPENDIX B

## METALLICITY CONVERSIONS: WORKED EXAMPLES

Three galaxies have metallicities of $12 + \log(\mathrm{O/H}) = 8.3$, 8.6, and 9.1 calculated using three different methods: KK04, PP04, and D02, respectively. To compare these galaxy metallicities with those derived by the SDSS team (T04), we convert the three galaxy metallicities into a metallicity base of T04.

For a galaxy with metallicity $12 + \log(\mathrm{O/H})_{\mathrm{KK04}} = 8.3$, the KK04 metallicity is calculated from the lower $R_{23}$ branch (see § A2.3). Table 3 gives the coefficients of the polynomial that converts a KK04 metallicity into a T04 base metallicity. Because our KK04 metallicity is from the lower branch, we use the linear relation for the lower branch conversion:

$$\begin{aligned}[\log(\mathrm{O/H}) + 12]_{\mathrm{T04}} &= -4.5710 + 1.53261[\log(\mathrm{O/H}) + 12]_{\mathrm{KK04}} \\ &\sim 8.2.\end{aligned}$$

To convert an original PP04 metallicity [$12 + \log(\mathrm{O/H})_{\mathrm{PP04}} = 8.6$] from O3N2 into a T04 base metallicity, Table 3 gives

$$\begin{aligned}[\log(\mathrm{O/H}) + 12]_{\mathrm{T04}} = &-738.1193 + 258.96730[\log(\mathrm{O/H}) + 12]_{\mathrm{PP04}} \\ &- 30.057050[\log(\mathrm{O/H}) + 12]^2_{\mathrm{PP04}} + 1.167937[\log(\mathrm{O/H}) + 12]^3_{\mathrm{PP04}} \\ &\sim 8.9.\end{aligned}$$

An original D02 metallicity $12 + \log(\mathrm{O/H})_{\mathrm{D02}} = 9.1$ cannot be converted into a T04 metallicity because this D02 abundance is above the valid range for our conversion from D02 into T04 (8.05–8.9).

As a final example, we convert a T04 abundance of $12 + \log(\mathrm{O/H})_{\mathrm{T04}} = 8.3$ into an M91 base metallicity. Note that the valid upper and lower branch ranges overlap for the conversion of T04 into M91, i.e., $8.2 < \log(\mathrm{O/H})_{\mathrm{T04}} < 9.2$ (upper branch) and $8.05 < \log(\mathrm{O/H})_{\mathrm{T04}} < 8.4$ (lower branch). At a T04 metallicity between $8.2 < \log(\mathrm{O/H})_{\mathrm{T04}} < 8.3$, the M91 $R_{23}$ calibration is reaching a local maximum and is insensitive to metallicity. In this regime, the M91 upper or lower branch should be selected based on the [N II]/[O II] or [N II]/H$\alpha$ ratio (§ A1). If the log ([N II]/H$\alpha$) ratio in our example galaxy is $-0.7$, then Figure 9 indicates that the metallicity is on the $R_{23}$ upper branch, and therefore the conversion from a T04 metallicity of $12 + \log(\mathrm{O/H})_{\mathrm{T04}} = 8.3$ into an M91 base metallicity is

$$\begin{aligned}[\log(\mathrm{O/H}) + 12]_{\mathrm{M91}} &= 404.1716 - 131.53250[\log(\mathrm{O/H}) + 12]_{\mathrm{T04}} \\ &\quad + 14.49175[\log(\mathrm{O/H}) + 12]^2_{\mathrm{T04}} - 0.5285842[\log(\mathrm{O/H}) + 12]^3_{\mathrm{T04}} \\ &\sim 8.6.\end{aligned}$$

## REFERENCES


Afflerbach, A., Churchwell, E., & Werner, M. W. 1997, ApJ, 478, 190
Allende Prieto, C., Lambert, D. L., & Asplund, M. 2001, ApJ, 556, L63
Aller, L. H., ed. 1984, Physics of Thermal Gaseous Nebulae (Dordrecht: Reidel)
Asplund, M., Grevesse, N., Sauval, A. J., Allende Prieto, C., & Kiselman, D. 2004, A&A, 417, 751
Baldry, I. K., et al. 2002, ApJ, 569, 582
Baldwin, J. A., Phillips, M. M., & Terlevich, R. 1981, PASP, 93, 5
Bell, E. F., & de Jong, R. S. 2000, MNRAS, 312, 497
———. 2001, ApJ, 550, 212
Boselli, A., Gavazzi, G., Donas, J., & Scodeggio, M. 2001, AJ, 121, 753
Bothun, G. D., Romanishin, W., Strom, S. E., & Strom, K. M. 1984, AJ, 89, 1300
Bresolin, F. 2006, preprint (astro-ph/0608410)
———. 2007, ApJ, 656, 186
Bresolin, F., Garnett, D. R., & Kennicutt, R. C. 2004, ApJ, 615, 228
Bresolin, F., Pietrzyński, G., Urbaneja, M. A., Gieren, W., Kudritzki, R.-P., & Venn, K. A. 2006, ApJ, 648, 1007
Brooks, A. M., Governato, F., Booth, C. M., Willman, B., Gardner, J. P., Wadsley, J., Stinson, G., & Quinn, T. 2007, ApJ, 655, L17
Brown, W. R., Geller, M. J., Kenyon, S. J., & Kurtz, M. J. 2006, ApJ, 647, 303
Bruzual, G., & Charlot, S. 2003, MNRAS, 344, 1000
Calura, F., Matteucci, F., & Menci, N. 2004, MNRAS, 353, 500
Cardelli, J. A., Clayton, G. C., & Mathis, J. S. 1989, ApJ, 345, 245
Carollo, C. M., & Lilly, S. J. 2001, ApJ, 548, L153
Davé, R., & Oppenheimer, B. D. 2007, MNRAS, 374, 427
Davis, M., & Peebles, P. J. E. 1983, ApJ, 267, 465
De Lucia, G., Kauffmann, G., & White, S. D. M. 2004, MNRAS, 349, 1101
Denicoló, G., Terlevich, R., & Terlevich, E. 2002, MNRAS, 330, 69 (D02)
de Rossi, M. E., Tissera, P. B., & Scannapieco, C. 2007, MNRAS, 374, 323
Díaz, A. I., & Pérez-Montero, E. 2000, MNRAS, 312, 130
Dopita, M. A., & Evans, I. N. 1986, ApJ, 307, 431
Dopita, M. A., Kewley, L. J., Heisler, C. A., & Sutherland, R. S. 2000, ApJ, 542, 224
Drory, N., Bender, R., & Hopp, U. 2004, ApJ, 616, L103
Edmunds, M. G., & Pagel, B. E. J. 1984, MNRAS, 211, 507
Erb, D. K., Shapley, A. E., Pettini, M., Steidel, C. C., Reddy, N. A., & Adelberger, K. L. 2006, ApJ, 644, 813
Ercolano, B., Bastian, N., & Stasinska, G. 2007, MNRAS, 379, 945
Esteban, C., García-Rojas, J., Peimbert, M., Peimbert, A., Ruiz, M. T., Rodríguez, M., & Carigi, L. 2005, ApJ, 618, L95
Esteban, C., Peimbert, M., García-Rojas, J., Ruiz, M. T., Peimbert, A., & Rodríguez, M. 2004, MNRAS, 355, 229
Esteban, C., Peimbert, M., Torres-Peimbert, S., & Rodríguez, M. 2002, ApJ, 581, 241
Ferland, G. J., Korista, K. T., Verner, D. A., Ferguson, J. W., Kingdon, J. B., & Verner, E. M. 1998, PASP, 110, 761
Finlator, K., & Dave, R. 2008, MNRAS, in press (arXiv:0704.3100)
Fioc, M., & Rocca-Volmerange, B. 1999, preprint (astro-ph/9912179)
Gallazzi, A., Charlot, S., Brinchmann, J., White, S. D. M., & Tremonti, C. A. 2005, MNRAS, 362, 41
García-Rojas, J., Esteban, C., Peimbert, A., Peimbert, M., Rodríguez, M., & Ruiz, M. T. 2005, MNRAS, 362, 301
García-Rojas, J., Esteban, C., Peimbert, M., Costado, M. T., Rodríguez, M., Peimbert, A., & Ruiz, M. T. 2006, MNRAS, 368, 253
Garnett, D. R. 2002, ApJ, 581, 1019
Garnett, D. R., Edmunds, M. G., Henry, R. B. C., Pagel, B. E. J., & Skillman, E. D. 2004a, AJ, 128, 2772
Garnett, D. R., Kennicutt, R. C., & Bresolin, F. 2004b, ApJ, 607, L21
Groves, B., Dopita, M., & Sutherland, R. 2006, A&A, 458, 405
Groves, B. A., Dopita, M. A., & Sutherland, R. S. 2004, ApJS, 153, 9
Hägele, G. F., Pérez-Montero, E., Díaz, Á. I., Terlevich, E., & Terlevich, R. 2006, MNRAS, 372, 293
Henry, R. B. C., & Worthey, G. 1999, PASP, 111, 919
Hoyos, C., Koo, D. C., Phillips, A. C., Willmer, C. N. A., & Guhathakurta, P. 2005, ApJ, 635, L21
Huchra, J., Davis, M., Latham, D., & Tonry, J. 1983, ApJS, 52, 89
Izotov, Y. I., Papaderos, P., Guseva, N. G., Fricke, K. J., & Thuan, T. X. 2006a, A&A, 454, 137
Izotov, Y. I., Stasińska, G., Guseva, N. G., & Thuan, T. X. 2004, A&A, 415, 87
Izotov, Y. I., Stasińska, G., Meynet, G., Guseva, N. G., & Thuan, T. X. 2006b, A&A, 448, 955
Jansen, R. A., Fabricant, D., Franx, M., & Caldwell, N. 2000a, ApJS, 126, 331
Jansen, R. A., Franx, M., Fabricant, D., & Caldwell, N. 2000b, ApJS, 126, 271
Kannappan, S. J., & Gawiser, E. 2007, ApJ, 657, L5
Kauffmann, G., et al. 2003, MNRAS, 341, 33 (K03)
Kennicutt, R. C., Bresolin, F., & Garnett, D. R. 2003, ApJ, 591, 801
Kewley, L. J., Brown, W. R., Geller, M. J., Kenyon, S. J., & Kurtz, M. J. 2007, AJ, 133, 882
Kewley, L. J., & Dopita, M. A. 2002, ApJS, 142, 35 (KD02)
Kewley, L. J., Dopita, M. A., Sutherland, R. S., Heisler, C. A., & Trevena, J. 2001, ApJ, 556, 121 (K01)
Kewley, L. J., Geller, M. J., & Jansen, R. A. 2004, AJ, 127, 2002
Kewley, L. J., Groves, B., Kauffmann, G., & Heckman, T. 2006, MNRAS, 372, 961 (K06)
Kewley, L. J., Jansen, R. A., & Geller, M. J. 2005, PASP, 117, 227
Kinman, T. D., & Davidson, K. 1981, ApJ, 243, 127
Kniazev, A. Y., Grebel, E. K., Hao, L., Strauss, M. A., Brinkmann, J., & Fukugita, M. 2003, ApJ, 593, L73
Kniazev, A. Y., Pustilnik, S. A., Grebel, E. K., Lee, H., & Pramskij, A. G. 2004, ApJS, 153, 429
Kobulnicky, H. A., Kennicutt, R. C., & Pizagno, J. L. 1999, ApJ, 514, 544
Kobulnicky, H. A., & Kewley, L. J. 2004, ApJ, 617, 240 (KK04)
Kobulnicky, H. A., & Zaritsky, D. 1999, ApJ, 511, 118
Kobulnicky, H. A., et al. 2003, ApJ, 599, 1006
Kong, X., & Cheng, F. Z. 2002, A&A, 389, 845
Köppen, J., Weidner, C., & Kroupa, P. 2007, MNRAS, 375, 673
Kroupa, P. 2001, MNRAS, 322, 231
Lamareille, F., Mouhcine, M., Contini, T., Lewis, I., & Maddox, S. 2004, MNRAS, 350, 396
Leitherer, C., et al. 1999, ApJS, 123, 3
Lequeux, J., Peimbert, M., Rayo, J. F., Serrano, A., & Torres-Peimbert, S. 1979, A&A, 80, 155
Liang, Y. C., Hammer, F., Flores, H., Elbaz, D., Marcillac, D., & Cesarsky, C. J. 2004, A&A, 423, 867
Liang, Y. C., Hammer, F., Yin, S. Y., Flores, H., Rodrigues, M., & Yang, Y. B. 2007, A&A, 473, 411
Liang, Y. C., Yin, S. Y., Hammer, F., Deng, L. C., Flores, H., & Zhang, B. 2006, ApJ, 652, 257
Lilly, S. J., Carollo, C. M., & Stockton, A. N. 2003, ApJ, 597, 730
López-Sánchez, Á. R., Esteban, C., García-Rojas, J., Peimbert, M., & Rodríguez, M. 2007, ApJ, 656, 168
Maier, C., Lilly, S. J., Carollo, C. M., Meisenheimer, K., Hippelein, H., & Stockton, A. 2006, ApJ, 639, 858

Maier, C., Lilly, S. J., Carollo, C. M., Stockton, A., & Brodwin, M. 2005, ApJ, 634, 849
Maier, C., Meisenheimer, K., & Hippelein, H. 2004, A&A, 418, 475
Martins, L. P., & Viegas, S. M. M. 2000, A&A, 361, 1121
Marzke, R. O., Huchra, J. P., & Geller, M. J. 1994, ApJ, 428, 43
Masegosa, J., Moles, M., & Campos-Aguilar, A. 1994, ApJ, 420, 576
Mathis, J. S., & Wood, K. 2005, MNRAS, 360, 227
McCall, M. L., Rybski, P. M., & Shields, G. A. 1985, ApJS, 57, 1
McGaugh, S. S. 1991, ApJ, 380, 140 (M91)
McGaugh, S. S., & de Blok, W. J. G. 1997, ApJ, 481, 689
Mouhcine, M., Bamford, S. P., Aragon-Salamanca, A., & Nakamura, O. 2006, MNRAS, 369, 891
Nagamine, K., Fukugita, M., Cen, R., & Ostriker, J. P. 2001, ApJ, 558, 497
Nagao, T., Maiolino, R., & Marconi, A. 2006, A&A, 459, 85
Osterbrock, D. E. 1989, Astrophysics of Gaseous Nebulae and Active Galactic Nuclei (Mill Valley: University Science Books)
Osterbrock, D. E., & Pogge, R. W. 1985, ApJ, 297, 166
Pagel, B. E. J., Edmunds, M. G., Blackwell, D. E., Chun, M. S., & Smith, G. 1979, MNRAS, 189, 95
Pagel, B. E. J., & Tautvaisiene, G. 1997, MNRAS, 288, 108
Papaderos, P., Guseva, N. G., Izotov, Y. I., Noeske, K. G., Thuan, T. X., & Fricke, K. J. 2006, A&A, 457, 45
Pei, Y. C., & Fall, S. M. 1995, ApJ, 454, 69
Peimbert, A., Peimbert, M., & Ruiz, M. T. 2005, ApJ, 634, 1056
Peimbert, M., Peimbert, A., Esteban, C., Garcia-Rojas, J., Bresolin, F., Carigi, L., Ruiz, M. T., & Lopez-Sanchez, A. R. 2007, Rev. Mex. AA Ser. Conf., 29, 72
Pettini, M. 2002, in ASP Conf. Ser. 253, Chemical Enrichment of Intracluster and Intergalactic Medium, ed. R. Fusco-Femiano & F. Matteucci (San Francisco: ASP), 181
Pettini, M., & Pagel, B. E. J. 2004, MNRAS, 348, L59 (PP04)
Pettini, M., Shapley, A. E., Steidel, C. C., Cuby, J.-G., Dickinson, M., Moorwood, A. F. M., Adelberger, K. L., & Giavalisco, M. 2001, ApJ, 554, 981
Pilyugin, L. S. 2001, A&A, 374, 412 (P01)
Pilyugin, L. S., & Thuan, T. X. 2005, ApJ, 631, 231 (P05)
Przybilla, N., Bresolin, F., Butler, K., Kudritzki, R. P., Urbaneja, M. A., & Venn, K. A. 2007, preprint (astro-ph/0703361)
Quireza, C., Rood, R. T., Bania, T. M., Balser, D. S., & Maciel, W. J. 2006, ApJ, 653, 1226
Rosenberg, J. L., Schneider, S. E., & Posson-Brown, J. 2005, AJ, 129, 1311
Rubin, V. C., Ford, W. K., & Whitmore, B. C. 1984, ApJ, 281, L21
Salpeter, E. E. 1955, ApJ, 121, 161
Savaglio, S., et al. 2005, ApJ, 635, 260
Schulte-Ladbeck, R. E., Miller, C. J., Hopp, U., Hopkins, A., Nichol, R. C., Voges, W., & Fang, T. 2003, preprint (astro-ph/0312069)
Shapley, A. E., Erb, D. K., Pettini, M., Steidel, C. C., & Adelberger, K. L. 2004, ApJ, 612, 108
Shields, G. A. 1990, ARA&A, 28, 525
Silva, L., Granato, G. L., Bressan, A., & Danese, L. 1998, ApJ, 509, 103
Simón-Díaz, S., Herrero, A., Esteban, C., & Najarro, F. 2006, A&A, 448, 351
Simpson, J. P., Colgan, S. W. J., Rubin, R. H., Erickson, E. F., & Haas, M. R. 1995, ApJ, 444, 721
Skillman, E. D., Kennicutt, R. C., & Hodge, P. W. 1989, ApJ, 347, 875
Somerville, R. S., Lemson, G., Kolatt, T. S., & Dekel, A. 2000, MNRAS, 316, 479
Somerville, R. S., & Primack, J. R. 1999, MNRAS, 310, 1087
Spergel, D. N., et al. 2003, ApJS, 148, 175
Stasińska, G. 1980, A&A, 84, 320
———. 2002, Rev. Mex. AA Conf. Ser., 12, 62
———. 2005, A&A, 434, 507
Sutherland, R. S., & Dopita, M. A. 1993, ApJS, 88, 253
Terlevich, R., Melnick, J., Masegosa, J., Moles, M., & Copetti, M. V. F. 1991, A&AS, 91, 285
Tissera, P. B., De Rossi, M. E., & Scannapieco, C. 2005, MNRAS, 364, L38
Tremonti, C. A., et al. 2004, ApJ, 613, 898 (T04)
Urbaneja, M. A., Herrero, A., Kudritzki, R.-P., Najarro, F., Smartt, S. J., Puls, J., Lennon, D. J., & Corral, L. J. 2005, ApJ, 635, 311
van Zee, L. 2000, ApJ, 543, L31
Veilleux, S., & Osterbrock, D. E. 1987, ApJS, 63, 295 (VO87)
Vila-Costas, M. B., & Edmunds, M. G. 1992, MNRAS, 259, 121
Wyse, R. F. G., & Silk, J. 1985, ApJ, 296, L1
Yin, S. Y., Liang, Y. C., Hammer, F., Brinchmann, J., Zhang, B., Deng, L. C., & Flores, H. 2007a, A&A, 462, 535
Yin, S. Y., Liang, Y. C., & Zhang, B. 2007b, in ASP Conf. Ser. 373, The Central Engine of Active Galactic Nuclei, ed. L. C. Ho & J.-M. Wang (San Francisco: ASP), 686
Zaritsky, D., Kennicutt, R. C., & Huchra, J. P. 1994, ApJ, 420, 87 (Z94)